nature nanotechnology

Article

https://doi.org/10.1038/s41565-026-02224-y

Dynamic delocalization of stress in brittle battery positive electrode active materials by shape-memory polymer nanocoating

Received: 29 January 2025

Accepted: 9 June 2026

Published online: 23 July 2026

Check for updates

Yutong Liu[1,2,11], Wenhua Zuo[3,11], Wei Wang[1,11], Cong Lin[4], Qingsong Weng[1], Yinggang Zhu[5], Kai Zhang[6], Ke Du[7], Haihui Ruan[1], Feng Pan[8], Xuejie Huang[9], Xiang Liu[10] ✉, Hailong Yu[9] ✉, Guohua Chen[2,5] ✉ & Qiang Liu[1,2] ✉

Stress-induced fractures are recognized as a primary cause of degradation in a wide range of positive electrode active materials during battery operation. However, the state-of-the-art mechanistic understanding and strategy development often overlook the brittle nature of these materials, as well as the dynamic and localized characteristics of mechanical stress during the charge and discharge cycles of the cell. Here we present a shape-memory polymer nanocoating method using initiated chemical vapour deposition to dynamically delocalize concentrated stresses in various positive electrode active materials, including Ni-rich layered oxides with different Ni contents and $LiFePO_4$. Fracture simulations and surface-to-bulk physicochemical characterizations collectively show that the balanced stiffness and deformability of the shape-memory polymer nanocoating on the positive electrode material effectively mitigate stress gradients and the consequent surface reconstruction, chemical heterogeneity and intergranular cracking during battery operation. In particular, when a polymeric nanocoated nickel-rich layered oxide positive electrode active material (90 at% of Ni) is tested in non-aqueous lithium metal coin cell configuration at 25 °C, the cells can be consistently charged and discharged over long cycles at moderate (for example, 1,000 cycles at 400 mA g^{-1}) and high (for example, 500 cycles at 1 A g^{-1}) specific currents.

Brittle fracture is a common cause of mechanical failure in natural and artificial engineering systems, including earthquakes[1], bone fractures[2] and battery performance decay[3,4]. In brittle materials, stress concentration can locally raise the stress by 10 to 100 times above the average[5,6], lowering the fracture initiation threshold[6]. In polycrystalline materials (for example, steels and Al_2O_3 ceramics), grain boundaries (GBs) are common sites where stress concentrates, making intergranular fracture a dominant failure mode[7,8]. Recent studies have identified intergranular cracking as a key degradation mechanism in various battery materials such as Si[9], Li transition metal oxides[10–12] and solid-state ceramic electrolytes[13]. In particular, polycrystalline Ni-rich $LiNi_{1-x-y}Co_xMn_yO_2$ (NCM, $x + y \leq 0.2$) positive electrode active materials exhibit pronounced intergranular microcracks during battery operation and manufacturing, contributing to rapid battery performance decay[10–12,14]. The microcracks are exacerbated at high Ni content (Ni ≥ 0.9)[14,15] and elevated upper cut-off potentials[11,16] (>4.3 V), posing challenges for deployment.

Such cracking originates from anisotropic lattice-level strain and stress induced by lithium insertion and extraction[14,17]. Despite

A full list of affiliations appears at the end of the paper. ✉e-mail: xiangliu@buaa.edu.cn; yuhailong@iphy.ac.cn; kechengh@ust.hk; keqiangliu@ust.hk

https://doi.org/10.1038/s41565-026-02224-y

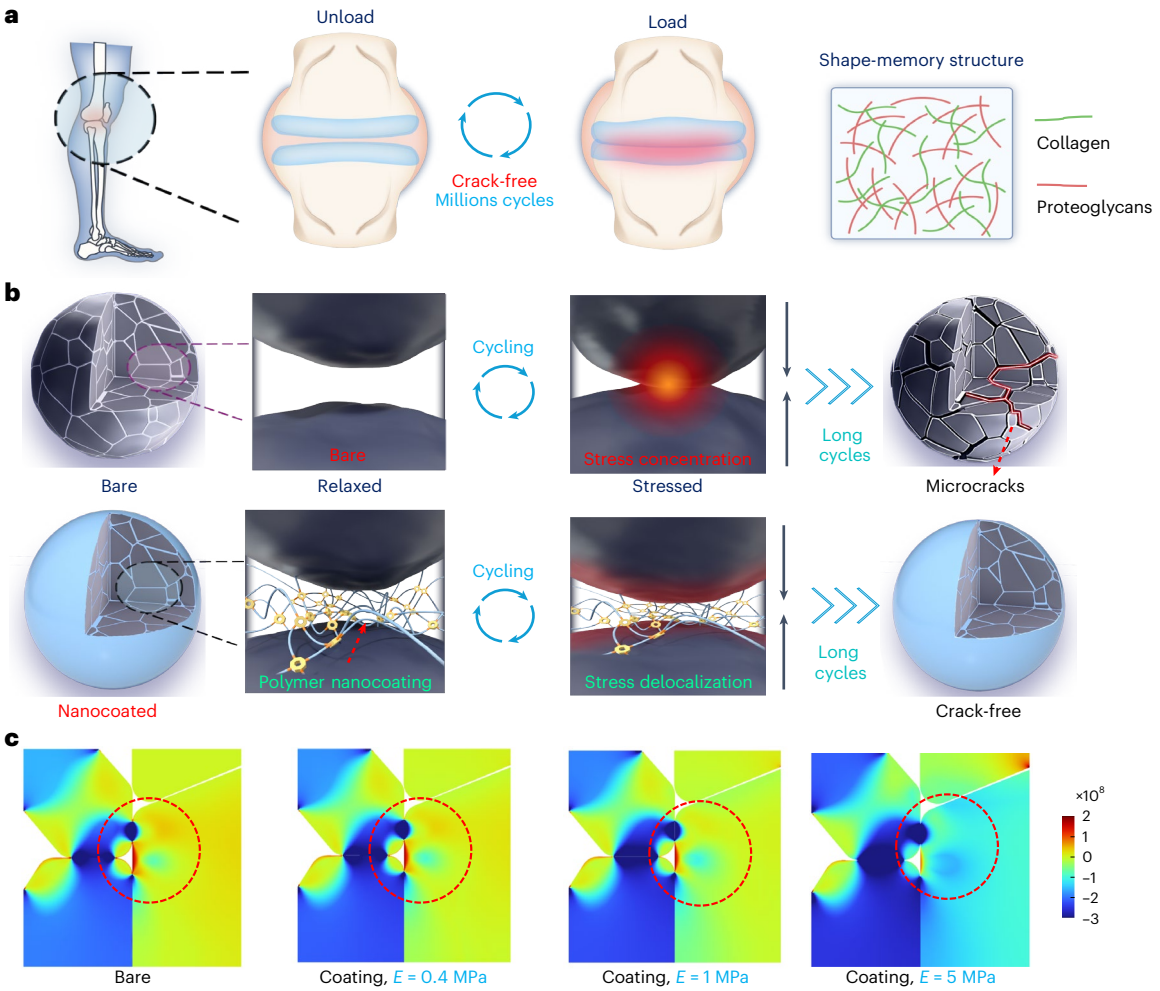


Fig. 1 | Stress delocalization strategy using SMP nanocoating at GBs of polycrystalline Ni-rich layered oxide materials. a, Illustration of the stress delocalization and shape-memory effect of cartilage in human joints. The cartilage exhibits a biological structure primarily composed of collagen fibres (green lines in the right panel) and proteoglycans (red lines in the right panel), enabling its shape-memory capability. **b**, Conceptual design diagram showing the application of SMP nanocoating at GBs of polycrystalline Ni-rich layered oxide particles. Stress concentrates severely on the GBs and induces microcracks in the bare material, highlighted by the red curves in the spherical particle (right panel). By contrast, the polymer nanocoating mimics cartilage-like behaviour to delocalize the intergranular stress and suppress microcrack formation. **c**, Phase-field simulations illustrate stress concentration behaviour in layered oxide with and without SMP nanocoating, emphasizing the effect of stress delocalization and its relationship to the stiffness of nanocoating. Increasing polymer nanocoating stiffness (*E*, Young's modulus from 0.4 MPa to 5 MPa) decreases stress localization and raises thresholds of crack initiation, demonstrating effective stress delocalization.

great efforts on mechanism understanding and strategy development, the dynamic[14,17] and localized characteristics[17–19] of the stress in brittle NCM materials are largely overlooked. Notably, the hardness and Young's modulus of NCM materials (80–200 GPa)[3,20] are comparable to those of typical brittle materials (glass, 70–150 GPa (ref. 21); concrete, 30–60 GPa (ref. 22)), underscoring their tendency to fracture under small strain. While conventional lattice element doping at the lattice level[20,23] improves the crystalline structure, this strategy does not address stress concentrations at GBs. Moreover, mechanical studies[17–19] show that localized stress at GBs decreases the fracture threshold. During battery redox cycling, lithium-ion gradients across NCM secondary particle electrode generate alternating compressive and tensile stresses[24–26], amplifying stress concentration—especially at high states of charge[11,16] and high current rates[16]. This understanding drove the development of GBs coating strategies using either soft polymers[27] or rigid inorganics[28]. However, these coatings often suffer a stiffness–deformability trade-off, limiting their ability to provide durable and reversible protection against dynamic mechanical stress during long-term cycling.

Nature offers inspiration for overcoming this limitation. In human joints, cartilage functions as a reversibly deformable interface between articulating bones, effectively dissipating stress and protecting brittle bones (Young's modulus ~20 GPa)[29] from fracture (Fig. 1a). This function is enabled by a densely entangled collagen–proteoglycans network that forms a robust hydrogel matrix with water within cartilage[30,31] (Fig. 1a, right panel). Under load, the soft components of cartilage—primarily water and proteoglycan gel—deform to increase the contact area and mitigate stress concentrations. Upon unloading, the entangled collagen microstructure facilitates shape recovery, allowing cartilage to endure millions of loading/unloading cycles without fracture[30,32]. This reversible deformation exemplifies efficient stress delocalization that protects brittle materials under dynamic and localized stress in biological systems.

Here, inspired by this dynamic stress delocalization mechanism (Fig. 1a), we propose the use of shape-memory polymers (SMPs) to mimic cartilage in delocalizing dynamic stress at the GBs of brittle NCM materials. SMPs are a class of polymers capable of deforming in response to external stimuli and returning to their original state upon

relaxation[33,34]. This on-demand response has garnered enormous interest in applications such as soft robotics[35], biomedical devices[34] and soft electronics[36]. Thus, we expect that a cyclically deformable SMP nanoscale coating at the GBs of NCM can effectively mitigate stress concentration in a dynamically responsive way, stabilizing the NCM microstructure during prolonged battery redox cycling, analogous to cartilage in joints (Fig. 1b). As a proof of concept, we applied SMP nanocoating to high Ni content NCM positive electrode active materials (Ni = 90.4 at%, $LiNi_{0.904}Co_{0.052}Mn_{0.044}O_2$; the chemical composition is shown in Supplementary Table 1, hereafter denoted as Ni90). As a result, the non-aqueous Li metal coin cells using SMP nanocoated Ni90 as the positive active material exhibit improved redox cycling stability compared with bare (uncoated) Ni90. Indeed, for one of the Li||nanocoated Ni90 coin cells tested, a specific discharge capacity retention of 91.6% after 1,000 cycles can be achieved at 400 mA g^{-1} and 25 °C within the potential range of 2.7–4.3 V (with the replacement of the Li metal negative electrode at the 510th cycle). The testing of another Li||nanocoated Ni90 coin cell delivers a final specific discharge capacity of 155.6 mAh g^{-1} after 500 cycles at 1 A g^{-1} and 25 °C within the potential range of 2.7–4.3 V with a calculated specific discharge capacity retention of 90.3% (no Li metal negative electrode replacement for this high specific current galvanostatic cycling test). To demonstrate the general applicability of the SMP nanocoating strategy, we also apply it to other positive electrode active materials such as polycrystalline $LiNi_{0.80}Co_{0.10}Mn_{0.10}O_2$ (NCM811) and $LiNi_{0.88}Co_{0.05}Mn_{0.07}O_2$ (Ni88), single-crystal $LiNi_{0.83}Co_{0.07}Mn_{0.10}O_2$ (NCM83) and $LiFePO_4$.

SMP nanocoating design

To validate the stress-delocalizing strategy via SMP nanocoating, we simulate the fracture behaviour of NCM materials with nanocoatings of varying stiffness using a phase-field fracture model, assuming that these layers could deform elastically. Finite element simulation results (Fig. 1c) reveal that deformable interlayers effectively delocalize stress concentrations, evidenced by the decrease in red coloration with polymer coating. Since the red colour indicates the tensile stress that initiates microcracks when exceeding a certain crack-onset threshold, its decrease reflects a drop in stress concentration. This is achieved through the stress delocalization effect of the SMP nanocoating, analogous to the function of cartilage in human joints. The simulations further suggest that increasing nanocoating stiffness as indicated by E values enhances stress delocalization and raises the crack-onset threshold (Extended Data Fig. 1; for further discussion, see Supplementary Note 1).

However, the trade-off between stiffness and deformability is a well-known phenomenon in materials. Polymer crosslinking offers a solution by integrating a deformable linear segment with a stiff crosslinking network, enabling both mechanical strength and shape-memory capability. This approach is widely adopted in the design of SMPs, where the crosslinked network serves as the 'shape-memory centres' for reversible shape recovery[33,37]. Following this principle, we designed crosslinked poly(butyl acrylate-co-1,3,5,7-tetravinyl-1,3,5,7-tetramethylcyclotetrasiloxane) (p(BA-V4D4)) as the SMP nanocoating material. Poly(butyl acrylate) (pBA), a well-known elastomer with linear chains, exhibits low stiffness (0.38 MPa as measured by atomic force microscopy (AFM); Supplementary Fig. 1a), which is desirable for deformation[38,39]. The 1,3,5,7-tetravinyl-1,3,5,7-tetramethylcyclotetrasiloxane (V4D4) crosslinker is incorporated to form a robust crosslinked network that improves the strength (4.91 MPa as measured by AFM; Supplementary Fig. 1a,b). Importantly, the crosslinked p(BA-V4D4) exhibits good shape-memory capability, as evidenced by the reversible deformation over 500 cycles (Supplementary Fig. 1c). Beyond mechanical properties, p(BA-V4D4) was selected for its reported Li^+ ionic conductivity, contributed by both pBA (~10^{-6} mS cm^{-1} at 20 °C)[39] and pV4D4 (~5.0×10^{-5} mS cm^{-1} at 25 °C)[40]. Linear sweep voltammetry measurements suggest that the p(BA-V4D4) is electrochemically stable as a positive electrode (Supplementary Fig. 2). With these desired mechanical and electrochemical properties, the p(BA-V4D4)-coated Ni90 enables improved cycling performance in cells compared with pBA- or pV4D4-coated Ni90 samples, when tested in a non-aqueous Li metal coin cell configuration (Supplementary Fig. 1d; more discussion on the strength, shape-memory capability and cell cycling stability in Supplementary Note 2).

To fabricate a p(BA-V4D4) layer at the GBs of NCM materials, we used an initiated chemical vapour deposition (iCVD; for process details, see Supplementary Note 3) nanocoating approach[41]. The success of crosslinking polymerization, based on the reaction scheme (Supplementary Fig. 3a,b), is confirmed by Fourier transform infrared spectroscopy (Supplementary Fig. 3c). High-resolution transmission electron microscopy (TEM) confirms the formation of a uniform and amorphous coating layer on the surface of Ni90 particles, with an estimated thickness of ~14 nm (Fig. 2a,b). The physicochemical properties of the p(BA-V4D4)-coated Ni90 particles were comprehensively characterized by scanning electron microscopy (SEM), high-energy X-ray diffraction (HEXRD), thermogravimetric analysis, X-ray photoelectron spectroscopy (XPS) and time-of-flight secondary ion mass spectrometry (TOF-SIMS) measurements. This set of characterization results (Supplementary Figs. 4 and 5) collectively validate the formation of a conformal p(BA-V4D4) nanocoating on Ni90 particles (detailed analyses in Supplementary Note 4).

Focused ion beam (FIB) technique is used to expose the primary particles for TEM and energy-dispersive spectroscopy (EDS) experiments to confirm the nanocoating on GBs. TEM images (Supplementary Fig. 6) of nanocoated Ni90 reveal distinct coatings at the GBs, in contrast to the clean and uncoated interfaces of the bare counterpart. More notably, while the bare Ni90 exhibits minimal Si (Fig. 2c) in EDS mapping of the Si element (a marker element originating from p(BA-V4D4)), the nanocoated Ni90 shows a conformal Si enrichment on the GBs (Fig. 2d). The Si signal on GBs is a strong proof confirming the success of p(BA-V4D4) nanocoating on GBs. EDS mappings (Supplementary Figs. 7 and 8) at additional randomly selected sites consistently confirm the presence of p(BA-V4D4) nanocoating at the GBs. Notably, this conformal polymer coating is observed not only on the outer surface but also on the core of the secondary particle (Extended Data Fig. 2). No discernible coating gradient is detected across the secondary particle, as evidenced by the uniform Si distribution in the EDS compositional analysis (Supplementary Table 2). This deep penetration of the p(BA-V4D4) coating into the core of the secondary particle is critical for achieving effective stress delocalization at the secondary particle level.

To evaluate the impact of the p(BA-V4D4) nanocoating on the mechanical properties of Ni90 particles, we conducted multiscale characterizations, including AFM for shallow surface analysis (<10 nm), micro-compression tests at the microscale and powder crushing tests at the macroscale. AFM nanoindentation mapping (5–8 nm depth) reveals a decrease in surface elastic modulus from 23.8 GPa for bare Ni90 to 7.83 GPa for nanocoated Ni90 (Figs. 2e,f and Supplementary Fig. 9). This suggests that the deformable p(BA-V4D4) nanocoating imparts ductility to the originally brittle Ni90 particles. A ductile nanocoating is expected to mitigate intergranular microcracking through stress delocalization. Indeed, the micro-compression (Fig. 2g and Supplementary Fig. 10) and crushing test results (Supplementary Fig. 11) validate the enhanced anti-cracking capability imparted by the polymer nanocoating (further discussion in Supplementary Note 5). Collectively, these mechanical assessments support our hypothesis that an SMP nanocoating effectively delocalizes interparticle stress, enhancing anti-cracking capability.

Electrochemical characterizations

The impact of the stress-delocalizing p(BA-V4D4) nanocoating on the electrochemical properties of Ni90-based positive electrodes is

https://doi.org/10.1038/s41565-026-02224-y

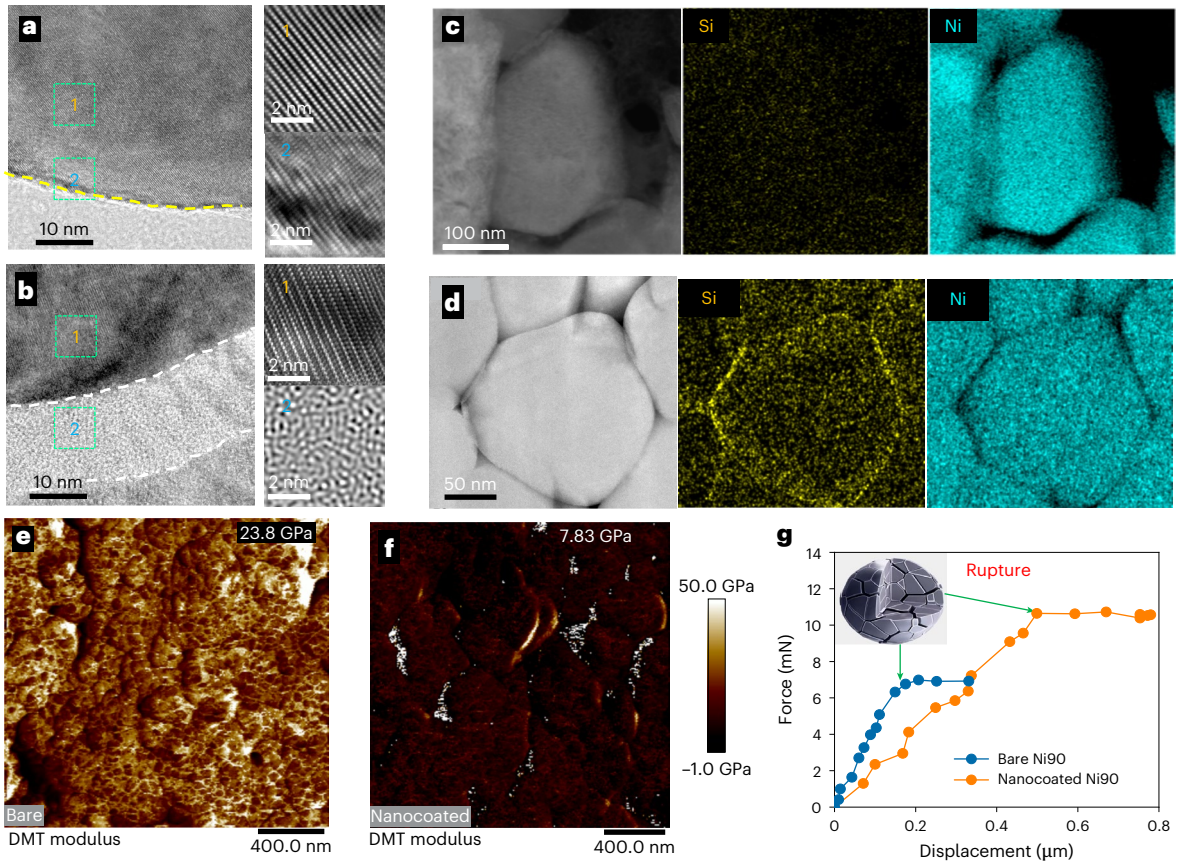


Fig. 2 | SMP nanocoating on Ni90 GBs enhances anti-cracking capability through stress delocalization. a,**b**, TEM images of the outer surfaces of bare (**a**) and nanocoated (**b**) Ni90 particles. A conformal and uniform nanocoating layer is observed on the surface of the nanocoated Ni90 particle. Insets: inverse fast Fourier transformation images of the marked regions of interest, revealing an amorphous layer on the surface of the nanocoated Ni90. **c**,**d**, TEM images and corresponding EDS mappings of Ni and Si for bare Ni90 (**c**) and nanocoated Ni90 (**d**) particles. Ni originates from the bulk Ni90, while Si comes from the p(BA-V4D4) molecule. The enrichment of the Si signal on the GBs confirms the presence of the p(BA-V4D4) polymer nanocoating on GBs. **e**,**f**, AFM mapping of the DMT modulus for bare (**e**) and nanocoated (**f**) Ni90 particles. The darker brown colour indicates lower DMT modulus (more deformable), while the brighter brown colour means higher DMT modulus (less deformable). The darker colour in **f** from the nanocoated Ni90 indicates increased surface deformability owing to the polymer nanocoating. **g**, Micro-compression force–displacement curves comparing bare and nanocoated Ni90 particles show enhanced rupture resistance in the nanocoated Ni90 sample compared with bare Ni90. The nanocoated Ni90 can withstand higher stress (9.56 mN) than bare Ni90 (4.55 mN) before cracking, suggesting that the nanocoating enhances the anti-cracking capability of Ni90.

investigated by testing in a non-aqueous coin cell configuration using Li metal as the negative electrode. The nanocoated Ni90 shows similar electrochemical behaviour to the bare counterpart, with slightly decreased polarization during initial cycles at 20 mA g^{-1} and 25 ± 2 °C (2.7–4.4 V) (Supplementary Fig. 12; extended discussion in Supplementary Note 6). The nanocoated Ni90 enables improved cycling stability in Li metal coin cells compared with Li||bare Ni90 cells. Specifically, the Li||nanocoated Ni90 shows a discharge capacity retention of 93.2% at 200 mA g^{-1} over 200 cycles (Fig. 3a–c) and maintains a stable average cell discharge potential (Supplementary Fig. 13). Long-term cycling data (Fig. 3d) are obtained from coin cells cycled at 400 mA g^{-1} and 25 °C ± 2 °C within the potential range of 2.7–4.3 V. The 1st discharge cycle of Li||nanocoated Ni90 cell at 400 mA g^{-1} shows a specific discharge capacity of 186.4 mAh g^{-1}, which decreases to 162.7 mAh g^{-1} at the 510th cycle. Electrochemical testing was paused at that cycle to replace the Li metal electrode before resuming redox cycling (details are provided in the Methods), and restarted the galvanostatic cycling test. At the 1,000th cycle, the coin cell still delivers a specific discharge capacity of 170.7 mAh g^{-1}, corresponding to a specific discharge capacity retention of about 91.6% from the first cycle and the last cycle at 400 mA g^{-1}. The differential capacity (dQ/dV) analysis (using the data shown in Fig. 3a,b) suggests that the nanocoating helps maintain the reversible H2–H3 phase transition of Ni90 during cell cycling (Supplementary Fig. 14; further discussion in Supplementary Note 7). Furthermore, the results of the galvanostatic intermittent titration technique (GITT) (Fig. 3e) and electrochemical impedance spectroscopy (EIS) (Supplementary Fig. 15 and Supplementary Table 3) collectively confirm that the polymer nanocoating stabilizes the positive electrode|electrolyte interface.

A common concern with coatings of active material particles is their potential to impede ion or electron transport, which may adversely affect battery rate performance. In our case, the cell using nanocoated Ni90 as positive electrode active material exhibits an improved rate capability compared with its bare counterpart, delivering high specific discharge capacities of 176.0 mAh g^{-1} and 166.8 mAh g^{-1} at specific currents of 1 A g^{-1} and 2 A g^{-1}, respectively (Fig. 3f; detailed discussion in Supplementary Note 8). The Li||nanocoated Ni90 coin cell enables a 90.3% specific discharge capacity retention over 500 cycles (Fig. 3g) at a high rate of 1 A g^{-1} (2.7–4.3 V) with initial and final specific discharge capacity values of 172.3 mAh g^{-1} and 155.6 mAh g^{-1} (Supplementary Fig. 16), respectively. All electrochemical cycling performance data in Fig. 3 have been repeated three times (Supplementary Figs. 17–19 and Supplementary Tables 4–6), exhibiting good reproducibility. The battery performances of the Li||nanocoated

https://doi.org/10.1038/s41565-026-02224-y

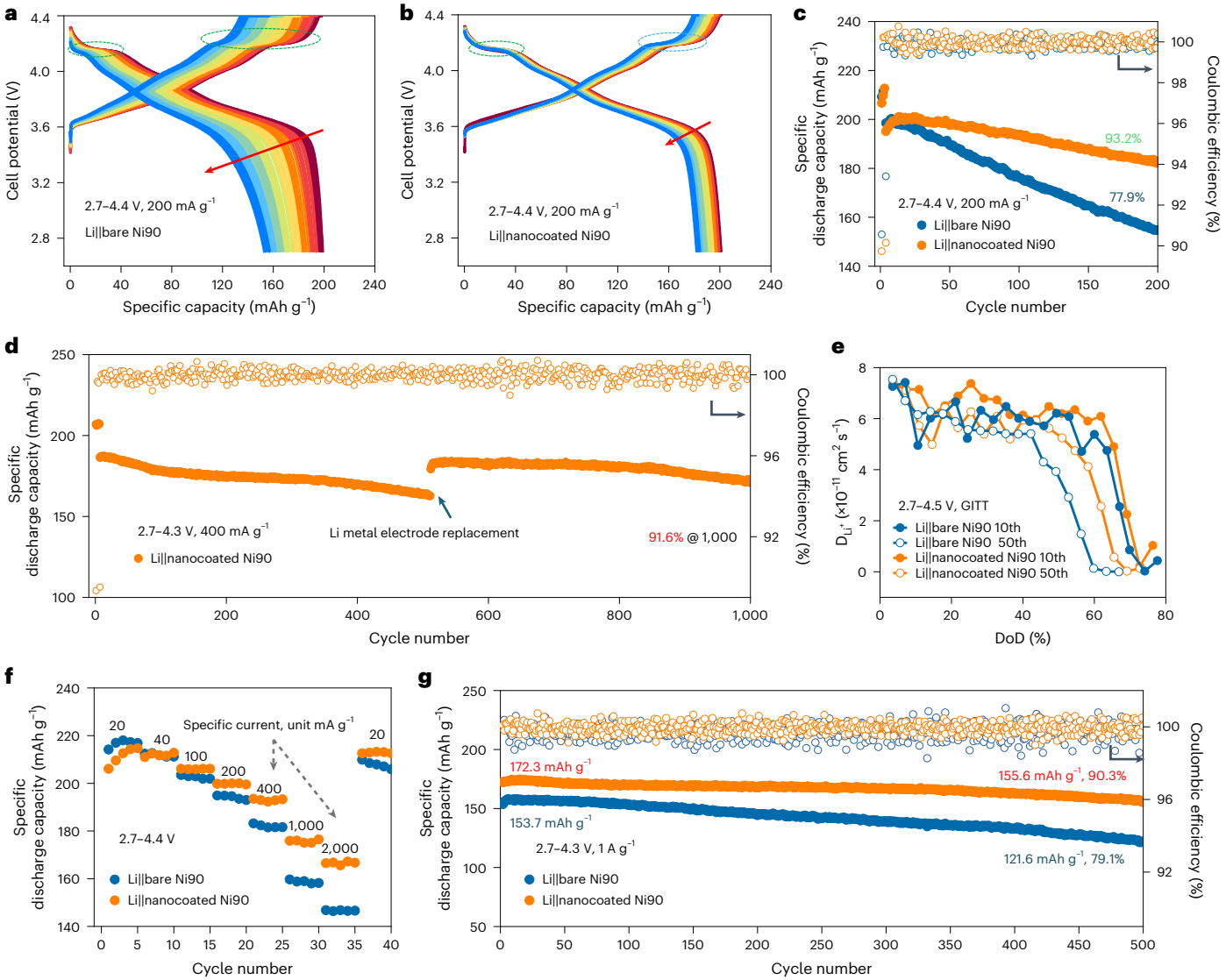


Fig. 3 | Electrochemical characterizations of the Li||nanocoated Ni90 and Li||bare Ni90 coin cells. a,**b**, Evolution of cell potential profiles during cycling at 200 mA g^{-1} between 2.7 V and 4.4 V for Li metal coin cells with the bare (**a**) and coated Ni90 (**b**) as active materials in positive electrodes. **c**, Cycling performance of Li||nanocoated Ni90 and Li||bare Ni90 coin cells at 200 mA g^{-1} in the 2.7–4.4 V cell potential range at 25 ± 2 °C. Retention values (77.9% and 93.2%, respectively) are calculated based on the first and last discharge specific capacities at 200 mA g^{-1} by taking the ratio of capacity at the final cycle to that at the first cycle (excluding the initial 3 cycles of formation at 20 mA g^{-1}). **d**, Long-term cycling performance at 400 mA g^{-1} in the 2.7–4.3 V cell potential range at 25 ± 2 °C. The Li metal negative electrode was replaced at the 510th cycle to minimize degradation effects from the Li metal, electrolyte and coin cell cases. The specific discharge capacity retention of 91.6% is calculated from the first to the last cycle at 400 mA g^{-1} by taking the ratio of capacity at the final cycle to that at the first cycle (excluding the initial 3 cycles of formation at 20 mA g^{-1}). **e**, Evolution of the Li^+ diffusion coefficient calculated from GITT measurements, for Li metal cells with the bare and nanocoated Ni90-based electrodes. The Li^+ diffusivity over cycling is measured at the 10th and 50th cycles. GITT was carried out from 4.5 V to 2.7 V to cover a broad range of depth of discharge (DoD). **f**, Galvanostatic rate capability comparing Li||bare Ni90 and Li||nanocoated Ni90 across various specific currents in the 2.7–4.4 V cell potential range at 25 ± 2 °C. The specific currents are indicated in the figure in terms of mA g^{-1}. **g**, High-rate cycling performance at 1 A g^{-1} over 500 cycles in the 2.7–4.3 V cell potential range at 25 ± 2 °C. The results show 90.3% specific discharge capacity retention (from 172.3 mAh g^{-1} to 155.6 mAh g^{-1}).

Ni90 coin cells are also well aligned with the state-of-the-art results reported in literature of non-aqueous lab-scale Li metal cells tested using various types of NCM-based positive electrode, exhibiting performance advantages in cycling stability (Supplementary Fig. 20 and Supplementary Tables 7 and 8).

In situ and ex situ physicochemical characterizations of Ni90-based electrodes

To elucidate the mechanism underlying the improved cycling stability of Li||nanocoated Ni90 coin cells against those with the bare Ni90, we investigate the crystalline structure of cycling-aged positive electrodes (after 200 cycles at 200 mA g^{-1}, in the cell potential range of 2.7–4.4 V and 25 ± 2 °C) via ex situ HEXRD measurements. The bare and nanocoated Ni90 materials after cycling exhibit similar spectral patterns and peak intensities, with only minor peak shifts (Supplementary Fig. 21), indicating that the structural framework is well maintained in both samples. These results suggest that phase changes are not the main cause of difference in battery performance. Therefore, we focus on strain accumulation, microcrack formation and surface degradation in the Ni90-based electrode materials.

To assess the impact of the SMP nanocoating on stress and strain evolution, we analyse the lattice parameter changes via in situ

https://doi.org/10.1038/s41565-026-02224-y

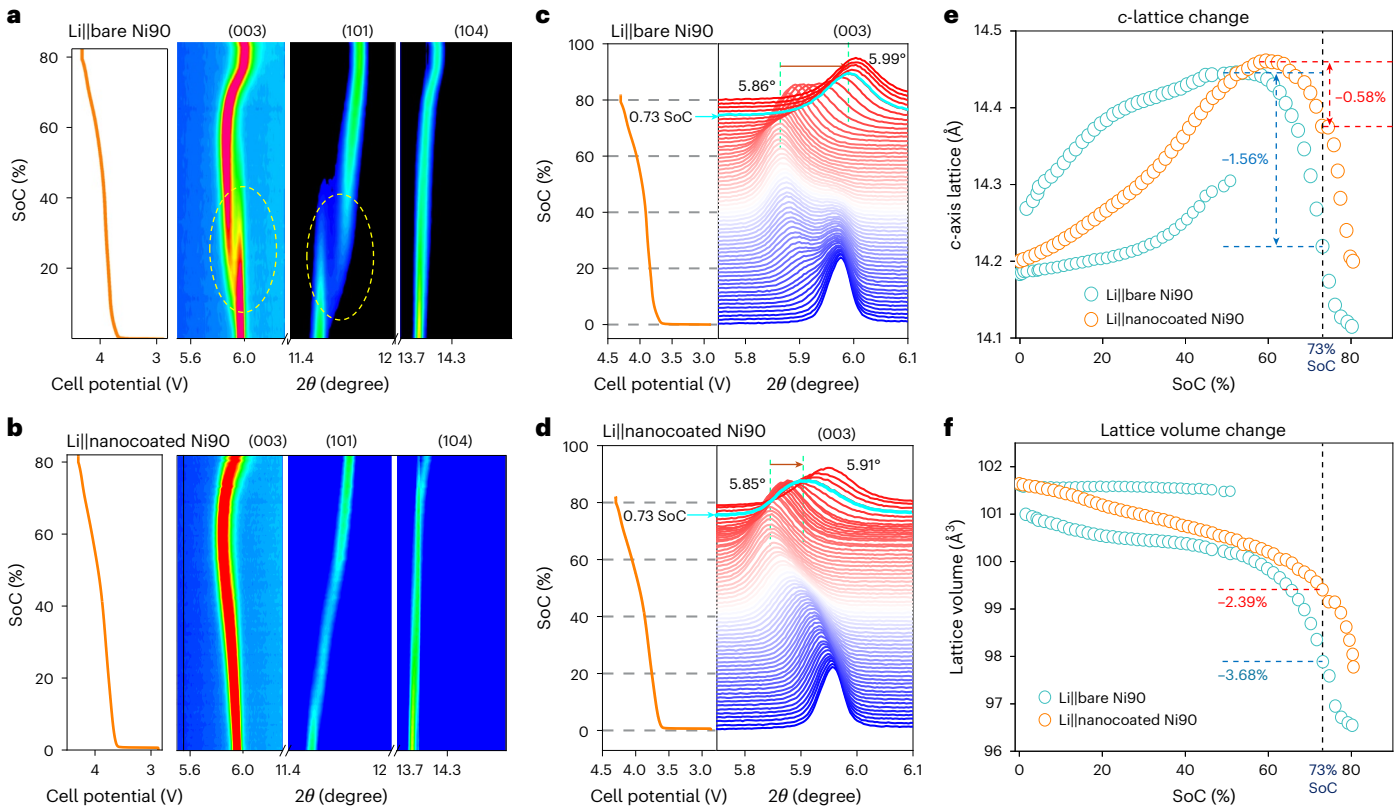


Fig. 4 | Lattice and volume changes characterized by in situ synchrotron XRD (wavelength 0.493168 Å) at 20 mA g^{-1} between 2.7 V and 4.3 V. **a**,**b**, Contour plots of the (003), (101) and (104) diffraction peaks obtained from in situ synchrotron XRD tests on Li||bare Ni90 (**a**) and Li||nanocoated Ni90 (**b**) cells. The bare Ni90 shows peak splitting, while the nanocoated sample exhibits continuous contour evolution. **c**,**d**, In situ evolution of the (003) diffraction peak for bare (**c**) and nanocoated (**d**) Ni90-based electrodes tested in Li metal cell configuration, showing decreased lattice contraction in the nanocoated sample. **e**, Evolution of the *c*-axis during charge from 2.7 V to 4.3 V. Reported values indicate the *c*-axis contraction from the peak value to 73% SoC (corresponding to the specific capacity of 200 mAh g^{-1}). The *c*-axis contraction is decreased from 1.56% in bare Ni90 to 0.58% in nanocoated Ni90. **f**, Lattice volume evolution with SoC during charge. Reported values indicate the volume changes from the highest point at 0% SoC to 73% SoC (corresponding to the specific capacity of 200 mAh g^{-1}). The volume change is suppressed from 3.68% for bare Ni90 to 2.39% for nanocoated Ni90.

synchrotron XRD during charge of the Li||nanocoated Ni90 and Li||bare Ni90 cells within the potential range of 2.7–4.3 V at a specific current of 20 mA g^{-1}. Both electrode materials exhibit the characteristic H1–M–H2–H3 phase transition during charge (Fig. 4a,b), consistent with existing literature[12,23,28]. However, unlike the continuous contour evolution in the nanocoated Ni90 (Fig. 4b), the bare Ni90 exhibits distinct peak splitting during evolution (Fig. 4a), indicative of a biphasic-like H1–H2 transition related to heterogeneous state of charge (SoC) distribution[26,42]. A more detailed discussion on the difference in phase evolution between the bare and nanocoated Ni90 samples is provided in Supplementary Note 9. To assess lattice strain, we track the evolution of the (003) peak from the highest value to 0.73 SoC (corresponding to a specific discharge capacity of 200 mAh g^{-1}). Here, θ represents the Bragg diffraction angle. Compared with a larger shift of 0.13° (Fig. 4c) in the bare Ni90, the nanocoated Ni90 exhibits a smooth 2θ shift of 0.06° (Fig. 4d). Rietveld refinement (details in Supplementary Tables 9–18) yields reliable lattice parameters with good fitting quality (Supplementary Figs. 22 and 23), revealing a similar shrinkage in the *a*-axis (Supplementary Fig. 24), but a notable difference in the *c*-axis (Fig. 4e). The nanocoated Ni90 exhibits a 'delayed' and decreased *c*-lattice shrinkage (0.58%) compared with bare Ni90 (1.56%), because of the Li$^+$-conductive p(BA-V4D4) nanocoating, which promotes a more uniform SoC distribution. Furthermore, the extent of volume change is also suppressed: from 3.68% for bare Ni90 to 2.39% for nanocoated Ni90 (Fig. 4f). These findings suggest that the nanocoating mitigates lattice and volume changes, likely owing to improved utilization of active material through a more uniform SoC distribution.

Full-field transmission X-ray microscopy (TXM) with X-ray absorption near edge structure (XANES) is a cutting-edge non-destructive synchrotron characterization that provides morphological, defects and valence-state information of battery materials[43]. Here we use three-dimensional (3D) TXM-XANES for the analysis of chemical and microstructural changes in both bare and nanocoated Ni90 particles because of electrochemical cycling-induced ageing. Ni K-edge white-line (WL) energy is used to evaluate the chemical homogeneity of the particles, with green representing Ni in a lower valence state (approaching +3) and red indicating Ni in a high valence state (approaching +4). To provide a quantitative reference for the TXM energy interpretation, ex situ bulk Ni K-edge hard X-ray absorption spectroscopy (hXAS) measurements are conducted on the same set of samples, alongside NiO (Ni^{2+}) and $LiNiO_2$ (Ni^{3+}) standards (Extended Data Fig. 3a). The bulk absorption edge energy (E_0) is determined from the inflection point of the main rising edge, corresponding to the second peak in the first derivative of the normalized Ni K-edge XANES spectrum (~8,342 eV). This value is 8,341.8 eV for both bare and nanocoated fresh samples (before cell assembly), indicating an average Ni valence state close to +3. After 200 cycles (200 mA g^{-1}, 2.7–4.4 V cell potential range, 25 ± 2 °C), the E_0 value shifts to 8,342.0 eV for the nanocoated sample and to 8,342.9 eV (a shift of 1.1 eV) for the bare sample (Extended Data Fig. 3b). This corresponds to a progressive valence shift of approximately 0.5–0.7 electrons, with the bare sample approaching

https://doi.org/10.1038/s41565-026-02224-y

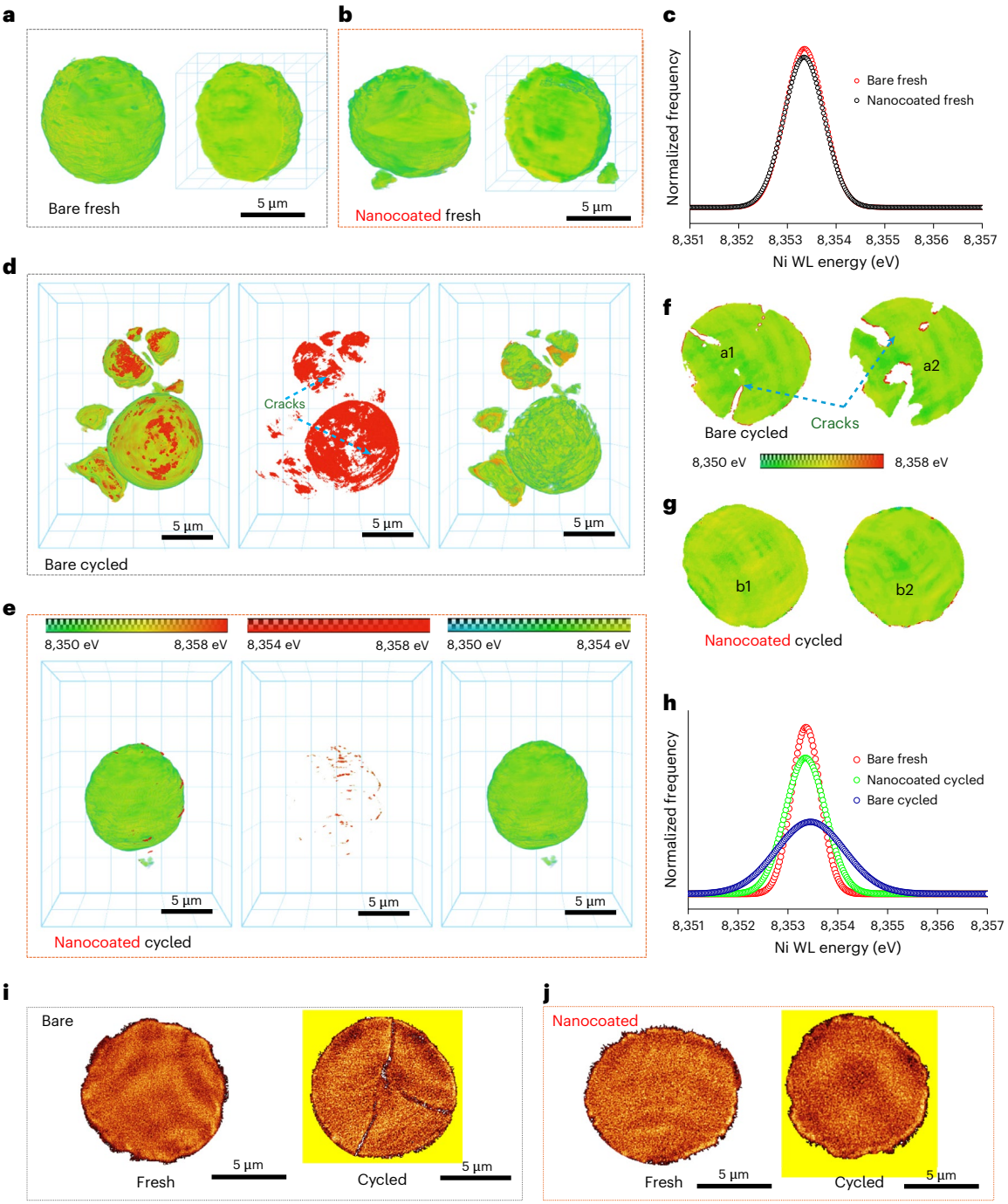


Fig. 5 | Microstructural and chemical state change of Ni90 particles before and after cycling in Li metal coin cells. The samples before cell assembly are referred to as 'fresh', while the cycled samples are referred to as 'cycled'. The cycled particle material samples are collected from positive electrodes that have been cycled in Li metal coin cells for 200 cycles at 200 mA g^{-1} and 25 ± 2 °C in the cell potential range of 2.7–4.4 V, followed by a final discharge at 20 mA g^{-1} to 2.7 V. **a**,**b**, 3D Ni K-edge TXM-XANES of fresh bare Ni90 (**a**) and fresh nanocoated Ni90 (**b**). **c**, Ni K-edge WL energy histogram based on approximately 10^6 pixels for fresh bare and fresh nanocoated Ni90 samples. **d**,**e**, 3D TXM-XANES results of cycled bare (**d**) and cycled nanocoated (**e**) Ni90 samples. Two representative particles are selected for slice image reconstruction: a1 and a2 for cycled bare Ni90, and b1 and b2 for cycled nanocoated Ni90. **f**,**g**, Ni WL energy maps from 3D XANES reconstructions of cycled bare (**f**) and cycled nanocoated (**g**) Ni90 samples. Particles a1 and a2 are from the cycled bare sample, where a1 is the same particle shown in **d** and a2 is a representative particle from another region. Particles b1 and b2 are from the cycled nanocoated sample; b1 is also shown in **e**, and b2 is a representative particle from a different region. **h**, Ni K-edge WL energy histogram of Ni90 particles from fresh bare, cycled bare and cycled nanocoated electrodes. **i**,**j**, Cross-sectional CT scan images acquired using 3D TXM techniques for bare (**i**) and nanocoated (**j**) Ni90 particles at both fresh and cycled states.

a Ni valence state of +3.5 or higher. Furthermore, the pre-edge region (~8,333–8,336 eV; Extended Data Fig. 3c), associated with the $1s \rightarrow 3d$ transition, exhibits distinct intensity variations among the samples. Notably, the cycled bare sample shows the highest pre-edge intensity, exceeding that of the fresh bare (before assembly), fresh nanocoated (before assembly) and cycled nanocoated samples. This enhancement suggests pronounced Ni 3*d*–O 2*p* hybridization and increased local distortion. By contrast, the nanocoated samples show more moderate pre-edge features, indicating suppressed over-oxidation and better preservation of the local coordination environment. These findings

https://doi.org/10.1038/s41565-026-02224-y

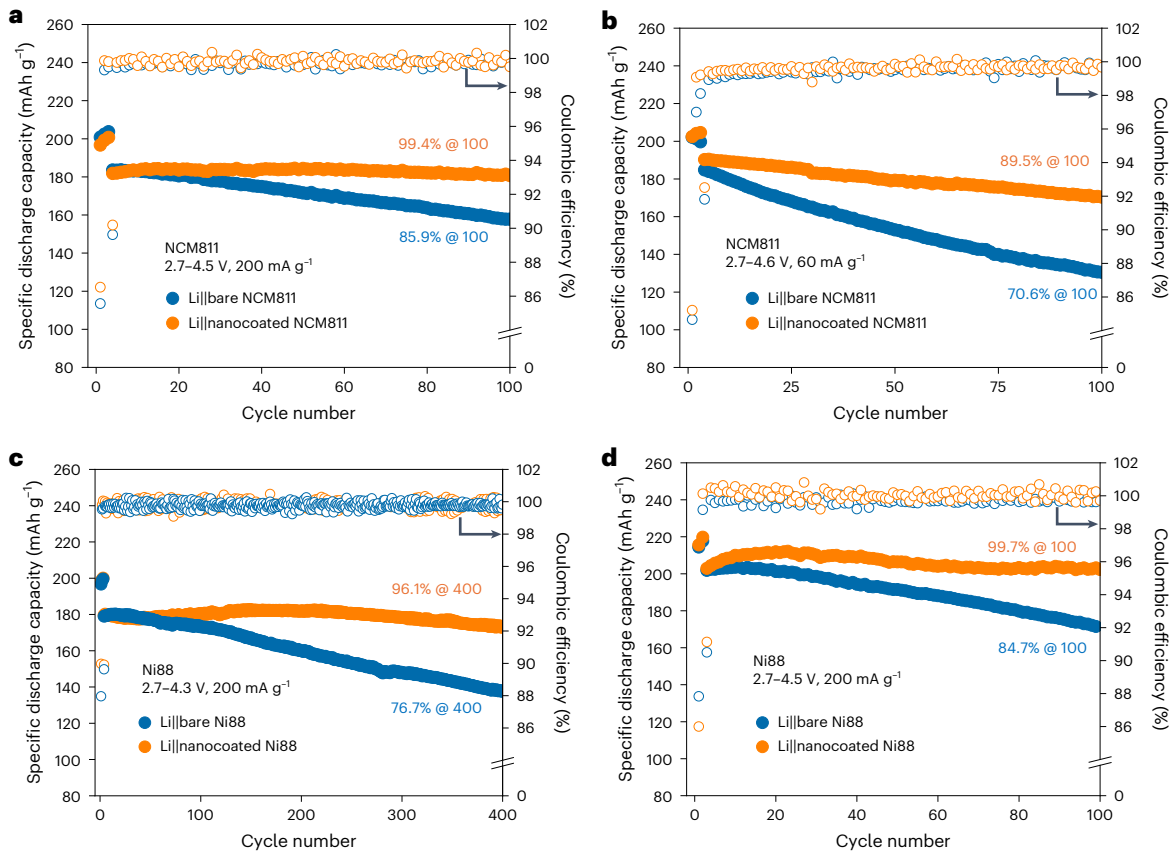


Fig. 6 | Effect of the SMP nanocoating on the cycling stability of Li metal coin cells containing layered positive electrode active materials with different Ni contents. a,**b**, Cycling performance of Li||NCM811 coin cells at two upper cut-off potentials: 4.5 V (**a**) and 4.6 V (**b**) at 200 mA g^{-1}. Retention values are calculated based on the first discharge specific capacities at high specific currents by taking the ratio of capacity at the final cycle to that at the first cycle (excluding the initial 3 cycles of formation at 20 mA g^{-1}). **c**,**d**, Cycling performance of Li||Ni88 coin cells at two upper cut-off potentials: 4.3 V (**c**) and 4.5 V (**d**) at 200 mA g^{-1} and 25 ± 2 °C. Retention values are calculated based on the first discharge specific capacities at high specific currents by taking the ratio of capacity at the final cycle to that at the first cycle (excluding the initial 3 cycles of formation at 20 mA g^{-1}).

align well with the FT-EXAFS results (Extended Data Fig. 3d), supporting the stabilizing role of the surface nanocoating during prolonged electrochemical cycling.

In the fresh state (before assembly), both bare Ni90 (Fig. 5a) and nanocoated Ni90 (Fig. 5b) particles exhibit a homogeneous Ni valence state distribution across the entire secondary particle, which aligns well with the bulk hXAS results. The Ni valence state histograms (Fig. 5c) show sharp peaks that are identical for both samples, confirming that the coating process does not alter the initial chemical state of the Ni90 particles. However, after 200 cycles, a notable red region is observed in both the 3D representation (Fig. 5d) and the 2D sliced (Fig. 5f) chemical mapping of the bare Ni90 particles, indicating substantial changes in the chemical state after redox cycling. These changes, associated with an increased proportion of high-valence Ni species, reflect severe performance degradation caused by contact loss and increased surface impedance, which hinders Ni from participating in reversible electrochemical reactions during prolonged battery cycling. By contrast, the comparative analysis of Ni K-edge WL energy ranges (Fig. 5e) reveals that the nanocoated Ni90 retains a smaller ratio of irreversible high-valence Ni species (8,354–8,358 eV, red regions), underscoring the ability of the nanocoating in preserving the reversible redox reaction of Ni during electrochemical cycling. These conclusions are more evident in the 2D representation results (Fig. 5g), in which the nanocoated Ni90 exhibits insignificant red regions, highlighting the beneficial chemical state stability provided by the p(BA-V4D4) nanocoating. Statistical analysis of the WL peak position confirms the high stability of nanocoated Ni90, with only slight changes in the chemical state (Fig. 5h).

3D TXM characterization is also an advanced tool for directly observing microcracks. The TXM computed tomography (CT) technique with a fixed incident X-ray energy of 8.2 keV has been utilized to further reveal the microcrack formation mechanisms during electrochemical cycling. Both TXM-XANES chemical mapping results (Fig. 5d–g) and cross-sectional TXM-CT results (Fig. 5i,j) demonstrate that the SMP nanocoating suppresses cracking at the Ni90 GBs. The TXM-CT result in Fig. 5i shows that after cycling, the bare Ni90 material exhibits a distinct microstructure compared with its fresh state (before cell assembly), exhibiting typical intergranular cracks that propagate from the core throughout the whole particle to the surface. Such major microcracks can be attributed to the dynamically concentrated stress at GBs[44,45] that accumulates and develops into cracks owing to the lack of a stress release mechanism in brittle NCM materials. By contrast, the nanocoated Ni90 particle largely maintains its integrated particle structure after cycling without observable microcracks (Fig. 5g,j). This microcrack difference is also verified by cross-sectional SEM images (Supplementary Fig. 25), confirming the role of the SMP nanocoating in crack suppression.

Despite the inherent structural stability of the bulk structure, surface deterioration[46–48] driven by the highly reactive Ni^{4+} in Ni-rich NCM remains a key challenge for long-term battery operation. Post-cycling TEM-EDS and TOF-SIMS 3D mapping confirm that the p(BA-V4D4) nanocoating remains intact at GBs after 200 cycles (Supplementary Fig. 26), which is key to long-term surface protection. Surface analyses using TEM-EDS (Extended Data Fig. 4a–d), XPS (Supplementary Figs. 27 and 28) and TOF-SIMS (Extended Data Fig. 4e–g and Supplementary Figs. 29

and 30) collectively indicate that the polymer nanocoating stabilizes the surface. Consequently, metal crosstalk is effectively suppressed, as shown by the diminished Ni, Co and Mn signals in XPS spectra of the Li metal negative electrode (Supplementary Fig. 31) obtained after electrochemical cycling with nanocoated Ni90 electrode in comparison with that from bare Ni90. Suppression of metal crosstalk is important for battery safety[49,50], as illustrated in Extended Data Fig. 4h. A detailed discussion of these characterization results can be found in Supplementary Note 10.

General applicability of the SMP nanocoating strategy to battery electrode active materials

To demonstrate the broad applicability of the stress-delocalizing strategy using SMP nanocoating, the p(BA-V4D4) nanocoating is further applied to other positive electrode materials, including three layered oxide positive electrodes with varying Ni contents and $LiFePO_4$. The bare and nanocoated active materials are fabricated into positive electrodes to be tested in non-aqueous Li metal coin cells. The results reveal that the nanocoating enhances the specific discharge capacity retention of Li||NCM811 cells increased from 85.9% for the bare NCM811 to 99.0% for the coated NCM811 after 100 cycles at 200 mA g^{-1} in the cell potential range of 2.7–4.5 V (Fig. 6a). Even when a high cut-off potential of 4.6 V is applied, the Li||coated NCM811 cell still maintains an 89.5% retention over 100 cycles at 60 mA g^{-1}, compared with the value of 70.6% for the Li||bare NCM811 (Fig. 6b). Battery performance improvement associated with the p(BA-V4D4) nanocoating can also be noticed for the Li||Ni88 cells during long-term cycling (Fig. 6c) and applying a high cut-off potential of 4.5 V (Fig. 6d). The p(BA-V4D4) nanocoating strategy also improves the cycling stability of the Li||single-crystal NCM83 and Li||$LiFePO_4$ coin cells (Extended Data Fig. 5a,b). These results confirm the applicability of the stress-delocalizing SMP nanocoating strategy across various positive electrode materials.

Conclusion

We prepared a cartilage-inspired SMP nanoscale coating to address the dynamic and localized stress characteristics of the brittle positive electrode active materials during battery operation. Our findings indicate that the coatings at GBs effectively enhance fracture resistance through a stress delocalization mechanism enabled by the reversible deformation of the polymer, as confirmed by fracture simulations and mechanical tests. Such a polymer nanocoating not only effectively maintains microstructure integration during redox cycling but also ensures a stable and Li^+-conductive surface, enabling the long-term cycling of Li metal coin cells for 1,000 cycles and good high specific current cyclability up to 1 A g^{-1}. Through a combination of synchrotron X-ray imaging, in situ diffraction, and ex situ post-cycling electron microscopy and spectroscopy analyses, we demonstrate that the microcracks induced by the dynamic and localized stress are effectively mitigated, enabling long-term cyclability for various positive electrodes including $LiFePO_4$ and Ni-rich positive electrodes with Ni contents of 80–90 at%. In conclusion, this work presents a technology to mitigate microcracks in battery positive electrode active materials by using an SMP with high stiffness and deformability as an adaptive stress dissipator. Further optimizations of the scalable iCVD nanocoating process and overall architecture of battery cell are necessary to make the proposed nanocoating approach a feasible strategy for use in practical large-area lithium-based batteries.

Online content

Any methods, additional references, Nature Portfolio reporting summaries, source data, extended data, supplementary information, acknowledgements, peer review information; details of author contributions and competing interests; and statements of data and code availability are available at https://doi.org/10.1038/s41565-026-02224-y.

References

1. Hatton, C., Main, I. & Meredith, P. Non-universal scaling of fracture length and opening displacement. *Nature* **367**, 160–162 (1994).
2. Taylor, D., Hazenberg, J. G. & Lee, T. C. Living with cracks: damage and repair in human bone. *Nat. Mater.* **6**, 263–268 (2007).
3. Stallard, J. C. et al. Mechanical properties of cathode materials for lithium-ion batteries. *Joule* **6**, 984–1007 (2022).
4. Ryu, H. H. et al. New class of Ni-rich cathode materials $Li[Ni_xCoyB_{1-x-y}]O_2$ for next lithium batteries. *Adv. Energy Mater.* **10**, 2000495 (2020).
5. Wiederhorn, S. Brittle fracture and toughening mechanisms in ceramics. *Annu. Rev. Mater. Sci.* **14**, 373–403 (1984).
6. Andrade, E. D. C. The mechanical properties of solids. *Nature* **148**, 520–525 (1941).
7. Rupert, T., Gianola, D., Gan, Y. & Hemker, K. Experimental observations of stress-driven grain boundary migration. *Science* **326**, 1686–1690 (2009).
8. Bammann, D. J. & Solanki, K. N. On kinematic, thermodynamic, and kinetic coupling of a damage theory for polycrystalline material. *Int. J. Plast.* **26**, 775–793 (2010).
9. de Vasconcelos, L. S. et al. Chemomechanics of rechargeable batteries: status, theories, and perspectives. *Chem. Rev.* **122**, 13043–13107 (2022).
10. Liu, T. et al. Origin of structural degradation in Li-rich layered oxide cathode. *Nature* **606**, 305–312 (2022).
11. Mu, L. et al. Oxygen release induced chemomechanical breakdown of layered cathode materials. *Nano Lett.* **18**, 3241–3249 (2018).
12. Zhang, R. et al. Compositionally complex doping for zero-strain zero-cobalt layered cathodes. *Nature* **610**, 67–73 (2022).
13. Dixit, M. B. et al. Polymorphism of garnet solid electrolytes and its implications for grain-level chemo-mechanics. *Nat. Mater.* **21**, 1298–1305 (2022).
14. Kondrakov, A. O. et al. Anisotropic lattice strain and mechanical degradation of high- and low-nickel NCM cathode materials for Li-ion batteries. *J. Phys. Chem. C* **121**, 3286–3294 (2017).
15. Xu, R., Sun, H., de Vasconcelos, L. S. & Zhao, K. Mechanical and structural degradation of $LiNi_xMn_yCo_zO_2$ cathode in Li-ion batteries: an experimental study. *J. Electrochem. Soc.* **164**, A3333–A3341 (2017).
16. Du, B. et al. Relieving the reaction heterogeneity at the subparticle scale in Ni-rich cathode materials with boosted cyclability. *ACS Appl. Mater. Interfaces* **14**, 6729–6739 (2022).
17. Li, W., Asl, H. Y., Xie, Q. & Manthiram, A. Collapse of $LiNi_{1-x-y}Co_xMn_yO_2$ lattice at deep charge irrespective of nickel content in lithium-ion batteries. *J. Am. Chem. Soc.* **141**, 5097–5101 (2019).
18. Xu, C., Reeves, P. J., Jacquet, Q. & Grey, C. P. Phase behavior during electrochemical cycling of Ni-rich cathode materials for Li-ion batteries. *Adv. Energy Mater.* **11**, 2003404 (2020).
19. Ryu, H.-H. et al. Microstrain alleviation in high-energy Ni-rich NCMA cathode for long battery life. *ACS Energy Lett.* **6**, 216–223 (2020).
20. Park, G.-T. et al. Introducing high-valence elements into cobalt-free layered cathodes for practical lithium-ion batteries. *Nat. Energy* **7**, 946–954 (2022).
21. Inaba, S., Fujino, S. & Morinaga, K. Young's modulus and compositional parameters of oxide glasses. *J. Am. Ceram. Soc.* **82**, 3501–3507 (2004).
22. Jurowski, K. & Grzeszczyk, S. The influence of concrete composition on Young's modulus. *Procedia Eng.* **108**, 584–591 (2015).
23. Wang, L., Liu, T., Wu, T. & Lu, J. Strain-retardant coherent perovskite phase stabilized Ni-rich cathode. *Nature* **611**, 61–67 (2022).

24. Xu, X. et al. Radially oriented single-crystal primary nanosheets enable ultrahigh rate and cycling properties of $LiNi_{0.8}Co_{0.1}Mn_{0.1}O_2$ cathode material for lithium-ion batteries. *Adv. Energy Mater.* **9**, 1803963 (2019).
25. Ju, P. et al. Designer particle morphology to eliminate local strain accumulation in high-nickel layered cathode materials. *ACS Energy Lett.* **8**, 3800–3810 (2023).
26. Romano et al. Synchrotron X-ray quantitative evaluation of transient deformation and damage phenomena in a single nickel-rich cathode particle. *Energy Environ. Sci.* **13**, 3556–3566 (2020).
27. Xu, G.-L. et al. Building ultraconformal protective layers on both secondary and primary particles of layered lithium transition metal oxide cathodes. *Nat. Energy* **4**, 484–494 (2019).
28. Zhao, C. et al. Suppressing strain propagation in ultrahigh-Ni cathodes during fast charging via epitaxial entropy-assisted coating. *Nat. Energy* **9**, 345–356 (2024).
29. Koester, K. J., Ager, J. W. III & Ritchie, R. O. The true toughness of human cortical bone measured with realistically short cracks. *Nat. Mater.* **7**, 672–677 (2008).
30. Fu, L. et al. Cartilage-like protein hydrogels engineered via entanglement. *Nature* **618**, 740–747 (2023).
31. Pueyo Moliner, A. et al. Restoring articular cartilage: insights from structure, composition and development. *Nat. Rev. Rheumatol.* **21**, 291–308 (2025).
32. Almarza, A. J. & Athanasiou, K. A. Design characteristics for the tissue engineering of cartilaginous tissues. *Ann. Biomed. Eng.* **32**, 2–17 (2004).
33. Xie, T. Tunable polymer multi-shape memory effect. *Nature* **464**, 267–270 (2010).
34. Lendlein, A. & Langer, R. Biodegradable, elastic shape-memory polymers for potential biomedical applications. *Science* **296**, 1673–1676 (2002).
35. Kim, S. U. et al. Broadband and pixelated camouflage in inflating chiral nematic liquid crystalline elastomers. *Nat. Mater.* **21**, 41–46 (2022).
36. Park, J. K. et al. Remotely triggered assembly of 3D mesostructures through shape-memory effects. *Adv. Mater.* **31**, e1905715 (2019).
37. Ni, C. et al. Shape memory polymer with programmable recovery onset. *Nature* **622**, 748–753 (2023).
38. Shi, L. et al. Highly stretchable and transparent ionic conducting elastomers. *Nat. Commun.* **9**, 2630 (2018).
39. Huang, J. et al. Ultrahigh energy-dissipation elastomers by precisely tailoring the relaxation of confined polymer fluids. *Nat. Commun.* **12**, 3610 (2021).
40. Reeja-Jayan, B. et al. A group of cyclic siloxane and silazane polymer films as nanoscale electrolytes for microbattery architectures. *Macromolecules* **48**, 5222–5229 (2015).
41. Heydari Gharahcheshmeh, M. & Gleason, K. K. Device fabrication based on oxidative chemical vapor deposition (oCVD) synthesis of conducting polymers and related conjugated organic materials. *Adv. Mater. Interfaces* **6**, 1801564 (2018).
42. Wang, J. et al. A kinetic indicator of ultrafast nickel-rich layered oxide cathodes. *ACS Energy Lett.* **8**, 2986–2995 (2023).
43. Zuo, W. et al. Microstrain screening towards defect-less layered transition metal oxide cathodes. *Nat. Nanotechnol.* **19**, 1644–1653 (2024).
44. Xu, J. et al. Understanding the degradation mechanism of lithium nickel oxide cathodes for Li-ion batteries. *ACS Appl. Mater. Interfaces* **8**, 31677–31683 (2016).
45. Wang, L. et al. High-energy all-solid-state lithium batteries enabled by Co-free $LiNiO_2$ cathodes with robust outside-in structures. *Nat. Nanotechnol.* **19**, 208–218 (2024).
46. Xu, C. et al. Bulk fatigue induced by surface reconstruction in layered Ni-rich cathodes for Li-ion batteries. *Nat. Mater.* **20**, 84–92 (2021).
47. Ryu, H.-H., Lim, H.-W., Lee, S. G. & Sun, Y.-K. Near-surface reconstruction in Ni-rich layered cathodes for high-performance lithium-ion batteries. *Nat. Energy* **9**, 47–56 (2023).
48. Jiang, M., Danilov, D. L., Eichel, R. A. & Notten, P. H. L. A review of degradation mechanisms and recent achievements for Ni-rich cathode-based Li-ion batteries. *Adv. Energy Mater.* **11**, 2103005 (2021).
49. Xu, H. et al. Impacts of dissolved Ni^{2+} on the solid electrolyte interphase on a graphite anode. *Angew. Chem. Int. Ed. Engl.* **61**, e202202894 (2022).
50. Zhan, C., Wu, T., Lu, J. & Amine, K. Dissolution, migration, and deposition of transition metal ions in Li-ion batteries exemplified by Mn-based cathodes—a critical review. *Energy Environ. Sci.* **11**, 243–257 (2018).

Publisher's note Springer Nature remains neutral with regard to jurisdictional claims in published maps and institutional affiliations.

Springer Nature or its licensor (e.g. a society or other partner) holds exclusive rights to this article under a publishing agreement with the author(s) or other rightsholder(s); author self-archiving of the accepted manuscript version of this article is solely governed by the terms of such publishing agreement and applicable law.

© The Author(s), under exclusive licence to Springer Nature Limited 2026

[1]Department of Mechanical Engineering, The Hong Kong Polytechnic University, Hung Hom, Kowloon, Hong Kong SAR, China. [2]Department of Chemical and Biological Engineering, The Hong Kong University of Science and Technology, Clear Water Bay, Kowloon, Hong Kong SAR, China. [3]State Key Laboratory for Physical Chemistry of Solid Surfaces, and Department of Chemistry, College of Chemistry and Chemical Engineering, Xiamen University, Xiamen, China. [4]Department of Applied Biology and Chemical Technology, The Hong Kong Polytechnic University, Hung Hom, Kowloon, Hong Kong SAR, China. [5]School of Energy and Environment, City University of Hong Kong, Kowloon Tong, Kowloon, Hong Kong SAR, China. [6]High Energy Photon Source, Institute of High Energy Physics, Chinese Academy of Sciences, Beijing, China. [7]School of Metallurgy and Environment, Central South University, Changsha, China. [8]School of Advanced Materials, Peking University Shenzhen Graduate School, Shenzhen, China. [9]Beijing National Center of Condensed Matter Physics, Institute of Physics, Chinese Academy of Sciences, Beijing, China. [10]School of Materials Science and Engineering, Beihang University, Beijing, China. [11]These authors contributed equally: Yutong Liu, Wenhua Zuo, Wei Wang. ✉e-mail: xiangliu@buaa.edu.cn; yuhailong@iphy.ac.cn; kechengh@ust.hk; keqiangliu@ust.hk

Methods

Positive electrode active materials preparation

Polycrystalline Ni90 samples were synthesized using $Ni_{0.9}Co_{0.05}Mn_{0.05}(OH)_2$ as precursor material (battery grade, BTR New Material Group). The precursor was manually mixed with lithium hydroxide monohydrate ($LiOH{\cdot}H_2O$, >98%, Sigma-Aldrich) using a mortar and pestle with a molar ratio of Li:(Ni + Co + Mn) being 1.04:1 under ambient air conditions at room temperature (25 ± 5 °C). The resulting mixture was subjected to a two-step thermal treatment: first, it was heated from room temperature to 550 °C at a ramp rate of 5 °C min^{-1} and held for 5 h; subsequently, it was further ramped at a rate of 5 °C min^{-1} to 825 °C and maintained at this value for 15 h in a tube furnace under continuous oxygen flow. After calcination, the sample was allowed to cool down naturally below 80 °C. The resulting calcined material was then pulverized and gently grounded using a mortar and pestle inside an argon-filled glovebox (MBRAUN, MB-Unilab Pro, Ar purity ≥99.999%, O_2 < 0.1 ppm, H_2O < 0.1 ppm) to avoid exposure to moisture. The fine powder was sealed inside a glass container and designated as Ni90.

The hydroxide precursors used for the synthesis of Ni88, NCM811 and single-crystal NCM83 are $Ni_{0.88}Co_{0.05}Mn_{0.07}(OH)_2$ (battery grade, BTR New Material Group), $Ni_{0.8}Co_{0.1}Mn_{0.1}(OH)_2$ (battery grade, BTR New Material Group) and $Ni_{0.83}Co_{0.10}Mn_{0.07}(OH)_2$ (battery grade, CNGR Advanced Material), respectively. For Ni88 and NCM811 samples, the high-temperature steps were set at 820 °C and 800 °C, respectively, while all other synthesis parameters remained identical to those used for Ni90. The single-crystal NCM83 sample was also prepared following a procedure similar to that used in the polycrystalline NCMs, with the high-temperature step at 850 °C for 12 h. After calcination, the sample was manually crushed using a pestle and mortar to obtain a fine powder, which was subsequently passed through a 400-mesh sieve to yield the final single-crystal NCM83 sample. The commercial $LiFePO_4$ material sample was obtained from MTI Corporation. All the Ni88, NCM811, single-crystal NCM83 and $LiFePO_4$ samples were stored in a glass container inside an argon-filled glovebox (MBRAUN, MB-Unilab Pro, Ar purity ≥99.999%, O_2 < 0.1 ppm, H_2O < 0.1 ppm) to avoid exposure to moisture.

iCVD p(BA-V4D4) polymer coating of Ni90

The iCVD process was used to coat Ni90 with p(BA-V4D4) polymer. A home-made iCVD coater similar to the one previously reported[27] was utilized for the polymer coatings. In this process, the 1,3,5,7-tetravinyl-1,3,5,7-tetramethylcyclotetrasiloxane (V4D4, >97%, Aladdin) monomer and butyl acrylate (BA, >97%, Aladdin) were introduced into the chamber at flow rates of 0.3 and 0.5 standard cubic centimetres per minute (SCCM), respectively, with nitrogen as the carrier gas at 4 SCCM. The di-tert-butyl peroxide (TBPO) initiator (98%, Aladdin) was introduced at 1 SCCM using a mass flow controller. To regulate the chamber pressure at 570 millitorr, a downstream feedback-control throttle valve (253B-1-40-1, MKS Instruments) was used. The reaction flask was immersed in a water bath to maintain a constant substrate temperature of 50 °C. The filament, heated resistively to 250 °C using a DC power supply, facilitated the thermolysis of the TBPO initiator to initiate the chain-reaction polymerization. The NCM samples were coated inside the reactor for 30 min, and the process was terminated by switching off the filament heating and stopping the flow of monomer and initiator.

Physicochemical characterizations

The metal composition in NCM materials was measured by inductively coupled plasma mass spectrometry (Agilent 710 Series). The chemical composition of the polymer coatings was analysed using Fourier transform infrared spectroscopy in transmission mode, conducted using a Bruker Vertex-70 instrument. Sample morphology was examined by SEM with Hitachi S-4700-II and TESCAN VEGA3 systems. High-resolution TEM was performed on a JEM-3200FS instrument operating at 300 kV and equipped with EDS for elemental analysis. FIB polishing was carried out using a Thermo Fisher SCIOS system to expose the primary particles and GBs. XPS measurements were conducted on a Thermo Fisher Nexsa spectrometer with Al Kα X-ray excitation. Binding energies were calibrated to the hydrocarbon C 1*s* peak at 284.8 eV. Ar^+ ion etching (2 kV, 2 μA, 45° incident angle) was performed with varying sputtering times (0 s, 100 s, 200 s, 300 s and 500 s). Surface and depth profiles of cycled positive electrodes were analysed by time-of-flight secondary ion mass spectrometry (TOF-SIMS 5-100, IONTOF) in negative polarity mode. For TOF-SIMS depth profiling, a Cs^+ beam (~60 nA at 1 keV) was used to sputter a 300 × 300 $μm^2$ area, followed by raster scanning with a Bi_3^+ analysis beam (~0.75 pA, 30 keV) over a 100 × 100 $μm^2$ area within the sputtered region. The TOF-SIMS sputtering rate, calibrated using a GaN reference, was 0.5 nm s^{-1}. Ex situ post-cycling positive electrode active material particles were collected from cycled electrodes for XPS and TEM analyses, while electrodes were used directly for TOF-SIMS analysis. The post-cycling positive electrode and active material particle sample preparation details are disclosed in the 'Post-cycling electrodes/active material particle samples preparation' section.

Mechanical property tests

The mechanical properties of both bare and nanocoated Ni90 samples were characterized using various techniques. Nanoindentation tests were conducted to assess the surface's force response at the nanoscale using a cantilever mounted on an atomic force microscope (Bruker Multimode 8 with a NanoScope V controller). The nanoindentation curves can be fitted using the Derjaguin–Muller–Toporov (DMT) model (Supplementary Fig. 32) to calculate the stiffness (Young's modulus) of the tested material, following the mathematical equations detailed in Supplementary Note 11. PeakForce Quantitative Nanomechanics (QNM) measurements were performed using a high-precision cantilever (RTESPA-525-30) mounted on an atomic force microscope (NanoScope IIIa/Dimension 3100). The DMT model was also used in the QNM measurement to quantify the strength as well. The mechanical stability of individual Ni90 particles was evaluated using a micro-compression tester (MCT-210, Shimadzu). The measurement was repeated on more than 20 particles of similar diameters (10–11 μm) to obtain a statistically meaningful result. In addition, crushing tests were performed with both the bare and nanocoated Ni90-based active material particles, using a universal tension/compression testing system with a pressure of 200 MPa (MTS810, MTS).

Electrochemical characterization

Electrode preparation. The positive electrodes were fabricated using a slurry-casting method. A mixture of active material, carbon black (C65, battery grade, MTI Corporation) and polyvinylidene difluoride (PVDF; ≥99.5%, MTI Corporation) was dispersed in *N*-methyl-2-pyrrolidone (NMP; >99.0%, Sigma-Aldrich) at a mass ratio of 90:6:4. As the polymer coating constituted only 0.34 wt% in the nanocoated Ni90 (calculated from the TGA result in Supplementary Fig. 4e), its mass was not considered in the slurry preparation or in specific capacity calculations. The mixing was performed using a mortar and pestle to prepare a uniform slurry, which was coated onto aluminium foil (>99.3%, thickness 5–16 μm, MTI Corporation) using a doctor blade (EQ-Se-KTQ-MH, MTI Corporation) inside an Ar-filled glovebox (MBRAUN, MB-Unilab Pro, Ar purity ≥99.999%, O_2 < 0.1 ppm, H_2O < 0.1 ppm). The coated laminates were taken out of the glovebox and dried in a vacuum oven overnight at 110 °C, and subsequently cut into electrodes with a diameter of 10 mm using a precision disc cutter (MSK-T-10, MTI Corporation). The average active material loading in the electrodes was controlled at 3–4 mg cm^{-2}. To improve the compactness of positive electrodes, electrodes were mechanically pressed using a pressure of 5 ± 0.5 MPa (hydraulic press YLJ-10T, MTI Corporation) to achieve an average porosity of 23–26% (cross-sectional SEM in Supplementary Fig. 33 and calculation details

in Supplementary Note 12). Notably, the polymer coating was found not to affect the rheology of the slurry, and therefore the slurry preparation and coating procedures were identical for bare and coated samples.

Coin cell assembly. The specific discharge capacity, rate capability and cycling performance were assessed using type 2025 coin cells (CR2025, SS304, MTI Corporation). The prepared positive electrodes were coupled with lithium metal negative electrodes (d = 15.6 mm, thickness = 0.45 mm, ≥99.90%, China Energy Lithium), Celgard 2325 separators (MTI Corporation, thickness, 25 µm; diameter, 19 mm; average pore size, ~30 nm; porosity, 39%) and non-aqueous electrolyte, which was sealed using a crimping machine (MIT MSK-110, pressure 400 ton m^{-2}) inside an Ar-filled glovebox (MBRAUN, MB-Unilab Pro, Ar purity ≥99.999%, O_2 < 0.1 ppm, H_2O < 0.1 ppm). In each cell, 30 µl of electrolyte solution was added using a pipette (Sartorius, 50 µl, BU-50F) with a 100 µl tip (Sartorius, 0.5–200 µl). The electrolyte solution consists of 1 M $LiPF_6$ (≥99.9%, China Duoduo Chem) dissolved in a solvent mixture of fluoroethylene carbonate (FEC; ≥99.9%, China Duoduo Chem) and ethyl methyl carbonate (EMC; ≥99.9%, China Duoduo Chem) (3:7 by volume), supplemented with 1 wt% lithium difluorophosphate (LiDFP; ≥99.9%, Shenzhen Capchem Technology). The salts used were dried at 55 °C on a hotplate (Thermo Scientific Cimarec+) for 12 h inside an Ar-filled (≥99.999%) glovebox (MBRAUN, MB-Unilab Pro, O_2 < 0.1 ppm, H_2O < 0.1 ppm) before use. All solvents used in electrolyte solution were treated by 4 Å molecular sieves (beads, 1.6–2.5 mm, Sigma-Aldrich, ~20% in volume) inside the same glovebox for 3 days before use. The molecular sieves were pre-activated by heating at 350 °C in a muffle furnace (Carbolite RFH 16/15) for 12 h.

Coin cell testing. Coin cells were cycled at various specific currents using a Landt CT2001 battery tester within defined potential windows. For standard electrochemical tests, the potential range between 2.7 V and 4.4 V was used, while a range of 2.7–4.3 V was adopted for long-term cycling (>200 cycles) to avoid degradation of the electrolyte solution at cell potentials higher than 4.3 V. For long-term cycling exceeding 500 cycles, the coin cells were disconnected from the tester at around 500 cycles to replace the Li metal negative electrodes before continuing the cycling test. This procedure was implemented to evaluate the intrinsic stability of the positive electrode active material, minimizing the influence of Li metal electrode degradation, consumption of electrolyte and corrosion of coin cell cases. To this end, the cells were carefully disassembled using an MTI MSK-110 crimping machine equipped with MSK-160D disassembly die set, inside the argon-filled glovebox, ensuring an inert atmosphere throughout the process. The aged Li metal electrodes were detached from the separators and replaced with pristine Li metal electrodes. Subsequently, new coin cell cases were assembled following the same protocol as described in the 'Coin cell assembly' section, with the addition of ~20 µl of freshly prepared electrolyte solution. The assembled coin cells were connected to the tester and then cycled under the same conditions before cell disconnection to 'continue' the long-term cycling. The specific capacity and specific current values reported in the article is based on the mass of the active material in the positive electrode. Unless otherwise specified, all electrochemical measurements were conducted in a temperature-controlled room maintained at 25 ± 2 °C. Linear sweep voltammetry measurements were conducted to evaluate the electrochemical stability of p(BA-V4D4) in lithium metal coin cells, using the p(BA-V4D4)-coated Al and uncoated Al as the positive electrodes. Data acquisition was conducted using a Metrohm Autolab PGSTAT204 potentiostat at a scan rate of 1 mV s^{-1}, sweeping from the open cell potential to 5 V at a temperature of 25 ± 2 °C. To prepare the p(BA-V4D4)-coated Al, Al discs (10 mm diameter) were coated in an iCVD coater for 30 min under the same conditions as those for the Ni90 coating (refer to the 'iCVD p(BA-V4D4) polymer coating of Ni90' section). Subsequently, both the p(BA-V4D4)-coated Al and uncoated Al discs were assembled as positive electrodes in lithium metal coin cells for linear sweep voltammetry measurements.

EIS measurement. EIS measurements were conducted on the two-electrode coin cells, with Li metal serving as both the counter and reference electrode. The EIS tests were performed at 60% SoC charged state using a Metrohm Autolab PGSTAT204 potentiostat. A sinusoidal potential perturbation of 5 mV was applied to probe the impedance response over a frequency range of 0.1 Hz to 10 kHz. To monitor the electrochemical impedance evolution during the cell cycling, EIS measurements were taken at 10th and 50th cycles. The cells were initially cycled for 3 times at 20 mA g^{-1} and 25 ± 2 °C with the cell potential range of 2.7–4.4 V to fully 'activate' the cell. Subsequently, they were further cycled at 200 mA g^{-1} under the same conditions. After 9 full cycles, the cells were charged to 60% SoC at a specific current of 40 mA g^{-1} for 3 h. Then, the cells were allowed to rest at open circuit potential for 8 h before EIS testing. The EIS data obtained at this stage are referred to as the 10th cycle EIS data. After acquiring the EIS data at the 10th cycle, the same cells were reconnected to the original testers to continue the cycle at 200 mA g^{-1} (2.7–4.4 V, 25 ± 2 °C) and stopped at the 49th cycle. The cells were charged to 60% SoC to acquire the EIS data at the 50th cycle, following the same procedure as for the 10th cycle. The EIS raw data were fitted using ZSimpWin (v3.6) software with the equivalent circuit model presented in Supplementary Fig. 15a. The suitability of the equivalent circuit model and detailed result interpretation are provided in Supplementary Note 13. All the EIS measurements were conducted in a temperature-controlled room maintained at 25 ± 2 °C.

GITT measurement. To monitor the electrochemical Li^+ diffusion coefficient evolution during the cell operation, GITT measurements were performed at the 10th and 50th cycles. The cells were first cycled 3 times at 20 mA g^{-1} and 25 ± 2 °C with the cell potential range of 2.7–4.5 V to fully 'activate' the cell, and then cycled at 200 mA g^{-1} (other conditions were unchanged). After 9 and 49 full cycles, respectively, the cycling process was paused to conduct GITT measurements using the programmed protocol. The data acquired are referred to as the 10th- and 50th-cycle GITT data in this paper. GITT measurements were conducted following established protocols[51,52], using Landt CT2001 testers. The test protocol was as follows: the cell was first charged at a specific current of 60 mA g^{-1} to a cell potential of 4.5 V, followed by constant-potential holding at 4.5 V until the specific current dropped to 10 mA g^{-1}. The upper cut-off potential of 4.5 V was intentionally selected to exceed the typical cut-off values used in this study (4.3 V and 4.4 V) to ensure that the subsequent discharge process encompassed both 4.4 V and 4.3 V states. After charging, a pulse discharge at 20 mA g^{-1} was applied to the cell for 30 min, followed by 1 h relaxation period without any current passing through the cell. The cycle, consisting of a pulse discharge and relaxation period, was repeated until the cell potential was below 2.7 V. The potential raw data during the GITT tests at the 10th and 50th cycles are presented in Supplementary Fig. 34. The fitting shows high-quality fitness (Supplementary Fig. 35, with average R^2 for all the fittings being above 0.99) with details and mathematical interpretation of the GITT presented in Supplementary Note 14. Unless otherwise specified, all GITT measurements were conducted in a temperature-controlled room maintained at 25 ± 2 °C.

Post-cycling electrodes/active material particle samples preparation

Post-cycling positive electrodes were collected from Li metal coin cells after 200 galvanostatic cycles at 200 mA g^{-1} and 25 ± 2 °C in the cell potential range of 2.7–4.4 V, followed by a final discharge to 2.7 V at 20 mA g^{-1}. The cells, in the fully discharged state, were disassembled inside an Ar-filled glovebox (MBRAUN, MB-Unilab Pro, O_2 < 0.1 ppm, H_2O < 0.1 ppm) using a crimping machine (MTI MSK-110) equipped with an MSK-160D disassembly die set. The positive electrodes were

carefully separated from the disassembled coin cell cases and separator using a pair of tweezers (RS PRO 130 mm) and rinsed in ~5 ml of dimethyl carbonate (DMC; Sigma-Aldrich, battery grade, ≥99.9%, acid <10 ppm, H_2O < 10 ppm) in a glass beaker. After 10 min, the electrodes were transferred to another beaker containing ~5 ml of fresh DMC. The washing step was repeated five times. The electrodes were then dried under Ar atmosphere in the glovebox for 30 min to obtain the cycled electrode samples. For the sample preparation of cycled Li metal negative electrodes for XPS analysis, the procedures are the same as those used for cycled positive electrodes preparation. To collect the active material particles, the as-prepared dried electrodes were gently scraped using a stainless-steel spatula. All disassembly, rinsing, scraping and drying steps were performed entirely inside the Ar-filled glovebox to prevent from air exposure.

For post-cycling TOF-SIMS analysis, the cycled electrodes were sealed in an aluminium–plastic laminate bag inside the glovebox for transporting them to TOF-SIMS sample preparation. The sample mounting process was performed under ambient air conditions with air exposure limited to <20 min counting from the opening of the aluminium–plastic laminate bag to the close of the TOF-SIMS sampling chamber. For post-cycling XPS measurements, particle samples were handled similarly, with air exposure kept below 10 min. For TEM analysis, particles were dispersed onto a TEM grid inside the glovebox and transferred in an airtight glass container sealed with a plastic lid, limiting air exposure to less than 5 min before loading into the TEM chamber. For TXM and XAS experiments, the cycled electrode active materials were sealed with Kapton film in an Ar-filled glovebox and transported in an airtight Ar container to the beamline. During sample preparation for data acquisition, the materials were exposed to ambient air for approximately 1 h (TXM) and 20 min (XAS), respectively.

HEXRD

The in situ HEXRD tests of the bare and nanocoated Ni90 positive electrodes were conducted at the I11 beamline, Diamond Light Source. The beam energy was 15 keV (λ = 0.493168 Å). During the in situ experiments, both bare and nanocoated Ni90 electrodes were charged in Li metal cells between 2.8 V and 4.3 V at 20 mA g^{-1} using a Neware battery tester. The cells were prepared by a modified procedure available in literature[53] (more details of cell assembly can be found in Supplementary Fig. 36). The wavelength and peak shape parameters were refined against a Si standard and are provided for each fit. Rietveld refinements of the in situ HEXRD diffraction patterns were performed using the GSAS-II software for the calculation of the lattice parameters. The specifications for Rietveld refinement of in situ HEXRD can be found in Supplementary Note 15. To address the splitting of in situ HEXRD peaks observed for bare Ni90, two sets of phase parameters (H1 and H2) were used to achieve the optimal fitting. Ex situ XRD measurements were performed using a wavelength of 0.82411 Å.

TXM tests

Full-field TXM experiments were performed at ID30-Transmission X-Ray Microscopic Beamline of High Energy Photon Source (https://cstr.cn/31138.02.HEPS.ID30). To ex situ analyse the cycled Ni90 particle samples, both bare and nanocoated Ni90 positive electrodes were subjected to 200 charge–discharge cycles at a rate of 200 mA g^{-1} in Li metal coin cell configuration within a potential window of 2.7–4.4 V at 25 ± 2 °C, followed by discharge to 2.7 V at 20 mA g^{-1}. The preparation details of the sample can be found in the 'Post-cycling electrodes/active material particle samples preparation' section. The cycled active material particle samples were sealed with Kapton film in an Ar-filled glovebox (99.999% Ar filled, O_2 < 0.1 ppm, H_2O < 0.1 ppm) for transportation within an airtight Ar container for TXM experiments (the samples have been exposed to air for ~1 h). The TXM datasets were reconstructed, registered and fitted using a specialized software package, TXM-Wizard[54]. The visualization and quantification of the 3D and 2D TXM results were obtained using the commercial Avizo software (2025 version; ThermoFisher Scientific). The energy calibration of the TXM-XANES measurements was performed using a Ni foil reference measured concurrently under identical beamline conditions.

XAS measurements

Ni K-edge XAS spectra were collected in the transmission mode. XAS data of metal foils and other reference materials were also collected in the transmission mode for bulk X-ray energy calibration and data alignment. Data processing was performed using the ATHENA software package. XAS measurements were performed on Ni90 particle samples at pristine (before electrode fabrication) and cycled state (cycling and sample preparation details can be found in the 'Post-cycling electrodes/active material particle samples preparation' section). The cycled active material particle samples were sealed with Kapton film in an Ar-filled glovebox (99.999% Ar filled, O_2 < 0.1 ppm, H_2O < 0.1 ppm) for transportation within an airtight Ar container to the beamline for XAS experiments (the samples have been exposed to air for ~20 min). The edge energy values (E_0) for bare and nanocoated positive electrode samples before and after cycling were determined from the inflection point of the main rising edge, corresponding to the second peak in the first derivative of the normalized XANES spectrum.

Crack simulation

The finite element simulation of crack was performed using a phase-field fracture model on four irregularly shaped particles as representative elements (Supplementary Fig. 37). The simulation details are elucidated in Supplementary Note 16.

Data availability

The datasets generated during and/or analysed during the current study are available from the corresponding authors on reasonable request. Correspondence and requests for materials should be addressed to G.C. or Q.L.

References

51. Xu, P. et al. Proton-exchange induced reactivity in layered oxides for lithium-ion batteries. *Nat. Commun.* **15**, 9842 (2024).
52. Liu, Q. et al. Approaching the capacity limit of lithium cobalt oxide in lithium ion batteries via lanthanum and aluminium doping. *Nat. Energy* **3**, 936–943 (2018).
53. Borkiewicz, O. J. et al. The AMPIX electrochemical cell: a versatile apparatus for in situ X-ray scattering and spectroscopic measurements. *J. Appl. Crystallogr.* **45**, 1261–1269 (2012).
54. Liu, Y. et al. TXM-Wizard: a program for advanced data collection and evaluation in full-field transmission X-ray microscopy. *J. Synchrotron Radiat.* **19**, 281–287 (2012).

Acknowledgements

We thank the ID30-Transmission X-Ray Microscopic Beamline of High Energy Photon Source (https://cstr.cn/31138.02.HEPS.ID30) for providing technical support and assistance in TXM data collection and analysis. The XAFS beam time was granted by the 1W1B beamline of Beijing Synchrotron Radiation Facility, Institute of High Energy Physics, Chinese Academy of Sciences. We thank the 1W1B-XAFS Beamline of Beijing Synchrotron Radiation Facility (https://cstr.cn/31109.02.BSRF.1W1B) and beamline staff for providing technical support and assistance in XAFS data collection and analysis, with special acknowledgement to S. Chu for data analysis. We thank Q. Sun, B. Zheng and C. Liu for their help during experiments at Beijing Synchrotron Radiation Facility. We also acknowledge support from Diamond Light Source for in situ HEXRD

experiments on the I11 beamline. We gratefully acknowledge Y. Ren of the City University of Hong Kong for assistance with the hXAS analysis. The iCVD set-up and design benefited from the guidance of K. K. S. Lau (Department of Chemical Engineering, Rowan University), whose support is gratefully acknowledged. The support from Michael De Volder (University of Cambridge) for HEXRD measurements is highly appreciated. We thank J.-l. Liu (MSc student, HKPolyU) for preparing the NCM samples and W. Zhao for FIB-TEM analysis. Additional thanks are extended to F. Xie for assistance with figure and schematic preparation, to L. An and X. Yu for discussion on electrochemical tests, and to P. Gao for discussions on polymer properties and for conducting electrical conductivity tests of the electrodes.

Author contributions

Q.L. and G.C. conceived the idea, designed the main experiment, secured the fundings and supervised the project. Y.L. developed the iCVD coating process in the laboratory under the supervision of Q.L. and G.C. Y.L. also performed the SMP coating, electrochemical tests, physicochemical analyses, data collection, data analysis, figure plotting and idea development. H.Y. designed the TXM experiment and performed part of data analysis. X.L. conducted nanoindentation and contributed to TXM and hXAS analysis. W.Z. carried out TXM and XAFS analysis and contributed to the interpretation of the results. C.L. performed the TEM characterization and XRD analysis. K.D. guided the NCM preparation and assisted with their structural analysis. W.W. and H.R. conducted the mechanical simulation tests. Q.W. and Y.Z. helped with materials synthesis and conducted their structural analysis. K.Z. guided the TXM experiments and 3D reconstruction. F.P. provided guidance on structural analysis and results discussion. X.H. provided guidance on TXM experiments and data analysis. Q.L., Y.L. and W.Z. wrote and revised the paper with the inputs from all co-authors, under the guidance of G.C. All authors participated in the analysis of experimental data and discussion of the results, as well as in writing and revision of the paper.

Funding

Q.L. discloses the support of this research from the Hong Kong Polytechnic University (HKPolyU) through the Start-up fund (ZZLJ) from the Department of Mechanical Engineering and Otto Poon Charitable Foundation (Q-CDA1). G.C. discloses the support from the Designated Donations from Bright Future Charitable Foundation (project number HKUST-R9976), the Guangdong-Hong Kong Joint Project (2021B1515130002) and the RGC/NSFC Joint Research Scheme (N_CityU549/22). X.H. discloses the support from the National Key R&D Program of China (grant number 2024YFB2504900). H.Y. discloses the support from the Youth Innovation Promotion Association CAS (grant number Y2023009). Y.L. and Q.W. disclose the postgraduate scholarship from the Hong Kong Polytechnic University. Y.Z. discloses the postgraduate scholarship from the City University of Hong Kong.

Competing interests

The authors declare no competing interests.

Additional information

Extended data is available for this paper at https://doi.org/10.1038/s41565-026-02224-y.

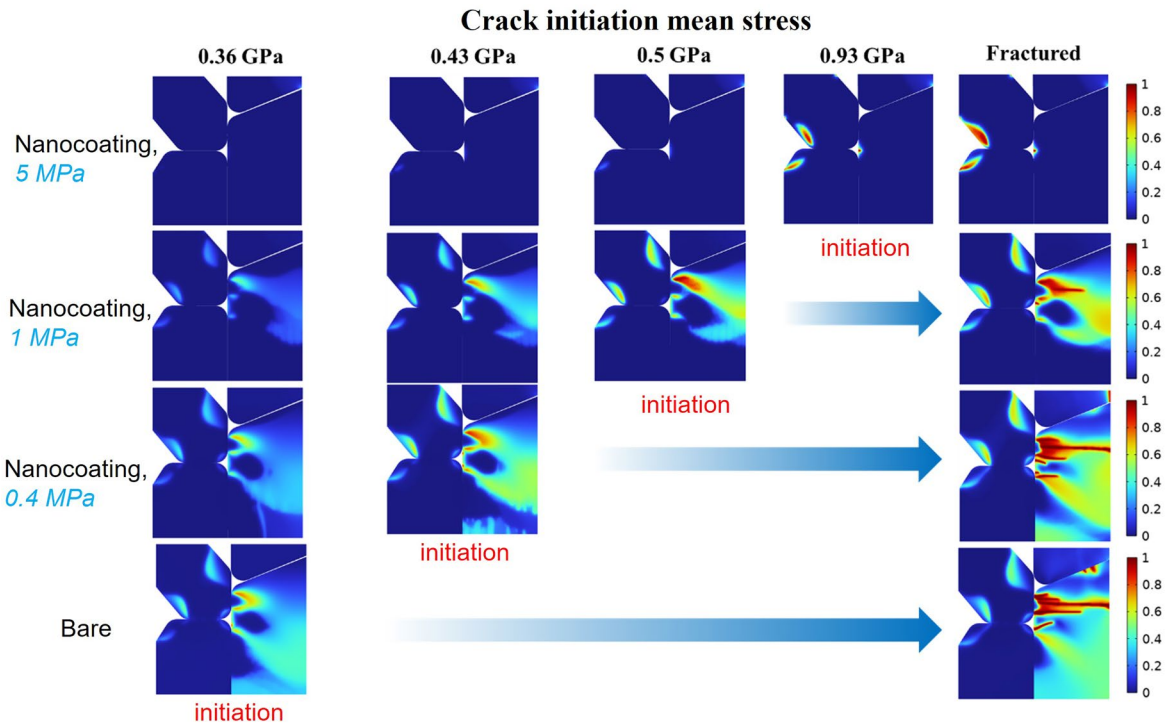
Supplementary information The online version contains supplementary material available at https://doi.org/10.1038/s41565-026-02224-y.

Correspondence and requests for materials should be addressed to Xiang Liu, Hailong Yu, Guohua Chen or Qiang Liu.

Peer review information *Nature Nanotechnology* thanks Thomas Barthelay, Matteo Bianchini and Yang Hu for their contribution to the peer review of this work.

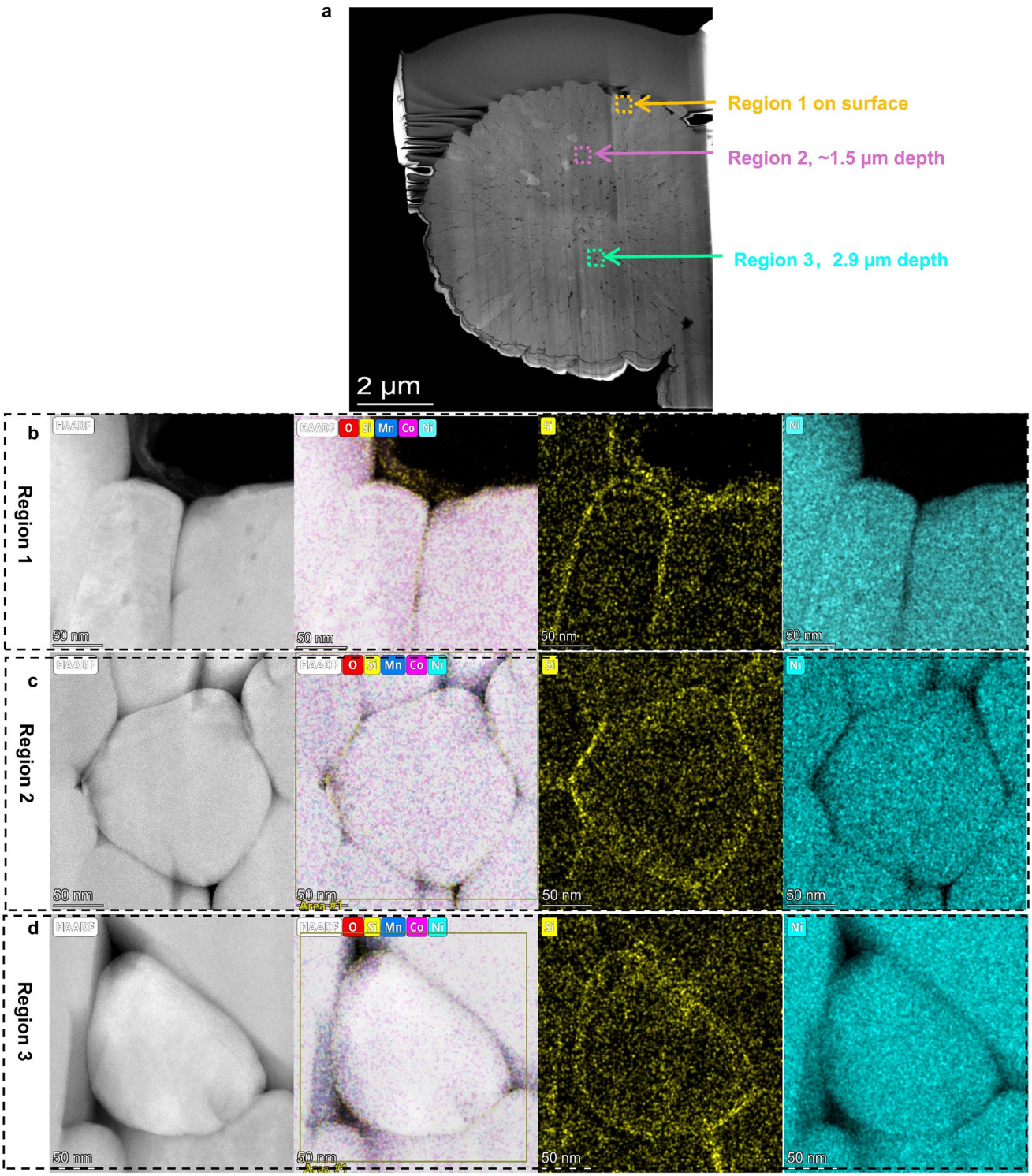
Reprints and permissions information is available at www.nature.com/reprints.

https://doi.org/10.1038/s41565-026-02224-y



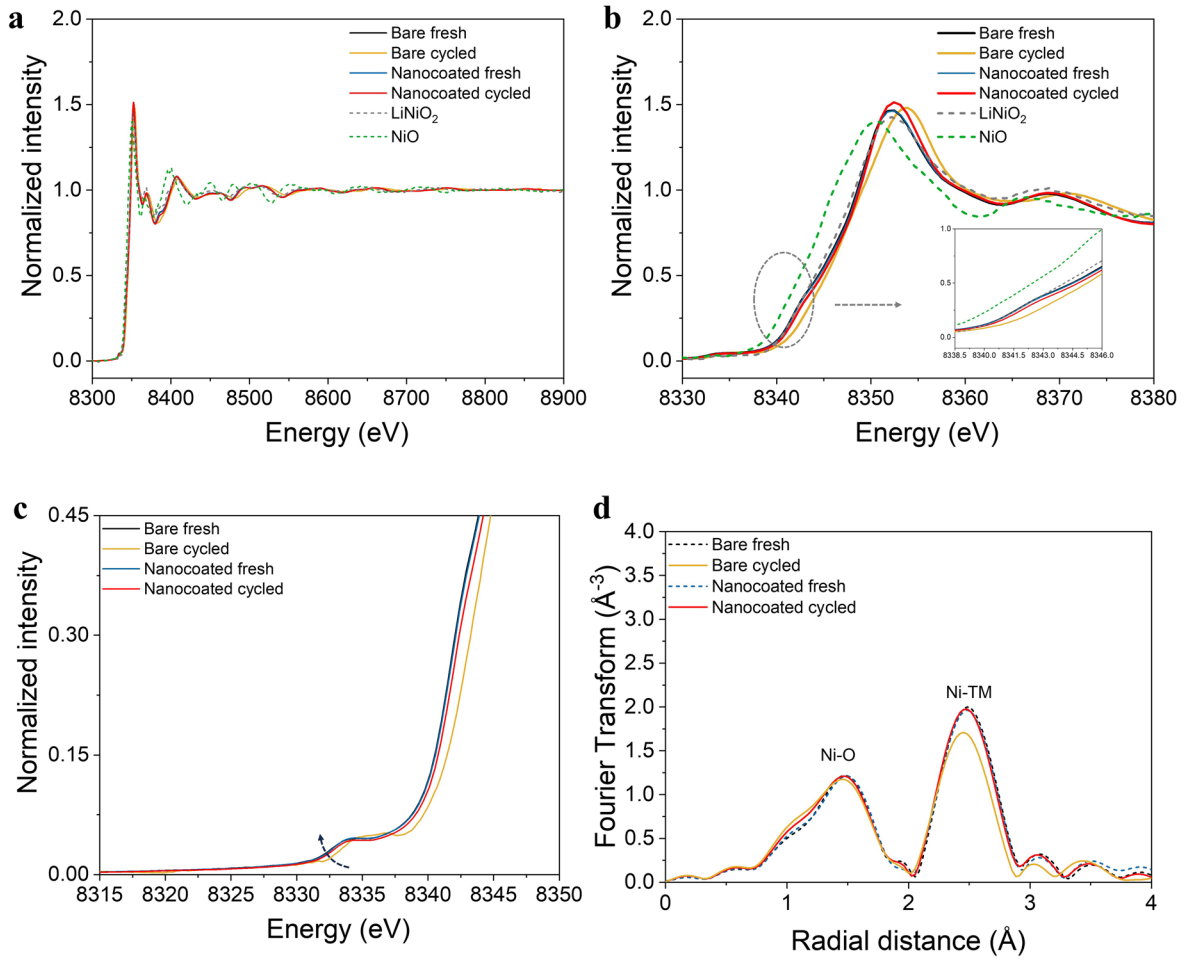
Extended Data Fig. 1 | The fracture phenomena for NCM without and with polymer grain boundary nanocoatings of various Young's moduli (0.4, 1, 5 MPa). The mean surrounding pressure on particles (denoted as $\bar{P}$, induced by lithium-ion insertion) required for crack initiation are 0.35, 0.43, 0.50, and 0.93 GPa for NCM without nanocoating and with nanocoatings of polymers with Young's modulus being 0.4, 1, and 5 MPa, respectively. When $\bar{P}$ exceed these values, cracks propagate in a brittle fracture mode, resulting in intergranular microcracks. Albeit the particles are the same, crack-onset $\bar{P}$ varies depending on the stiffness of the nanocoating polymers. Without the polymer nanocoating, the critical value of $\bar{P}$ is 0.36 GPa (the bottom row); once exceeding this value, cracks are initiated, propagated and branched in nanoseconds. A soft nanocoating polymer with a Young's modulus of 0.4 MPa does not help particles resist cracking with the $\bar{P}$ slightly increased to 0.43 GPa (the third row from top). When the Young's modulus of the polymer increases to 1 MPa, crack nucleation is delayed to a larger $\bar{P}$ of 0.5 GPa (the second row from top). When the Young's modulus of the nanocoating polymer is increased to 5 MPa, the particles are almost intact even when $\bar{P}$ rises to 0.93 GPa (the top row). While the further expansion of particles leads to some damage on boundaries, the damaged area remains small, which is distinct from the cases with much lower Young's modulus. These results demonstrate that nanocoatings with polymers of higher Young's moduli effectively suppress intragranular cracking in NCM particles.

https://doi.org/10.1038/s41565-026-02224-y



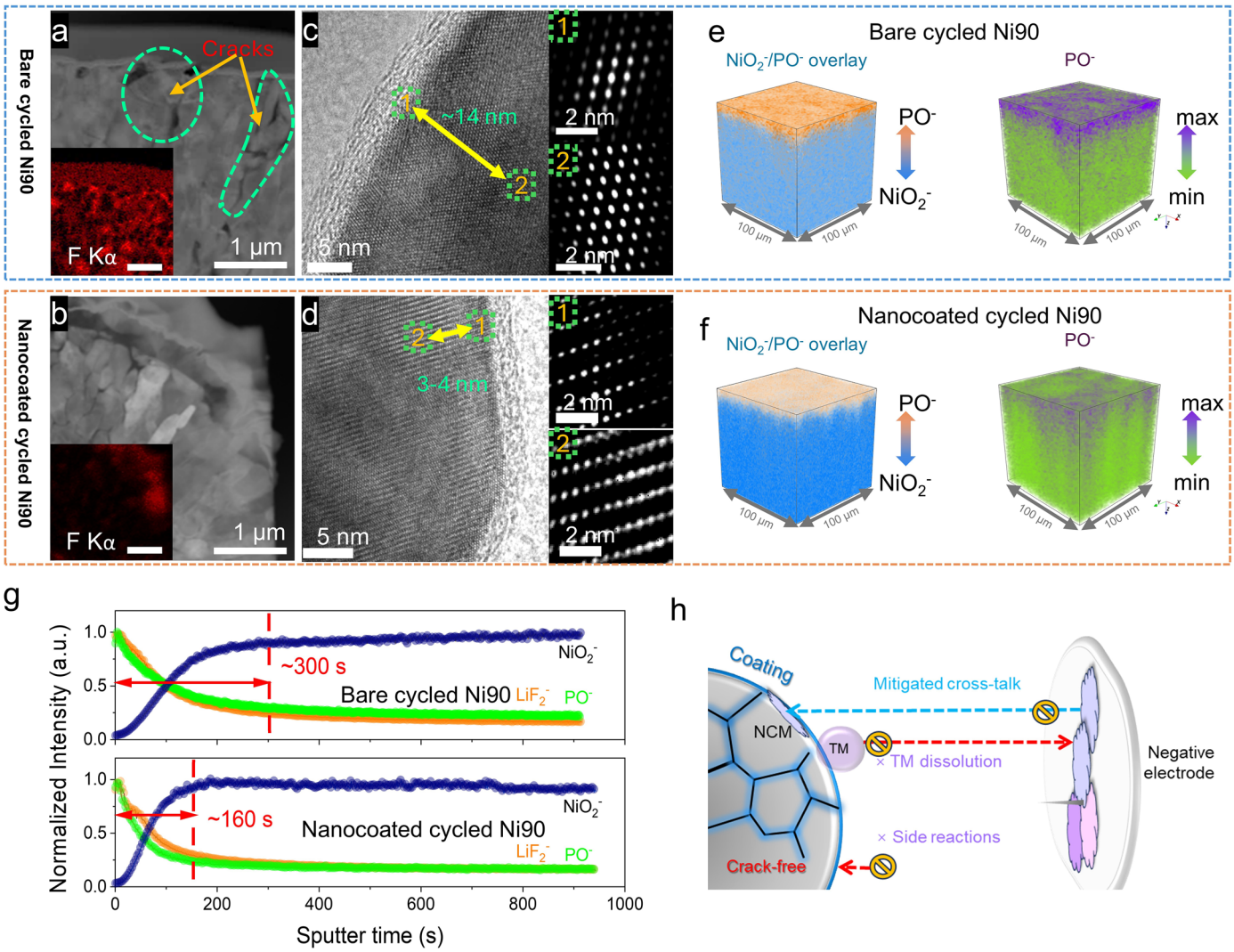
Extended Data Fig. 2 | TEM and EDS mapping on different regions from the surface to the core of a secondary particle of nanocoated Ni90. a, The sample, prepared using the FIB technique, showing the three regions selected for TEM and EDS analysis. **b-d**, TEM images (left) and corresponding EDS mappings for mixed elements (O, Si, Mn, Co, Ni), Si, and Ni (from left to right). Note that the Si element from the moiety of p(BA-V4D4) can serve as a signature element for the polymer nanocoating.

https://doi.org/10.1038/s41565-026-02224-y



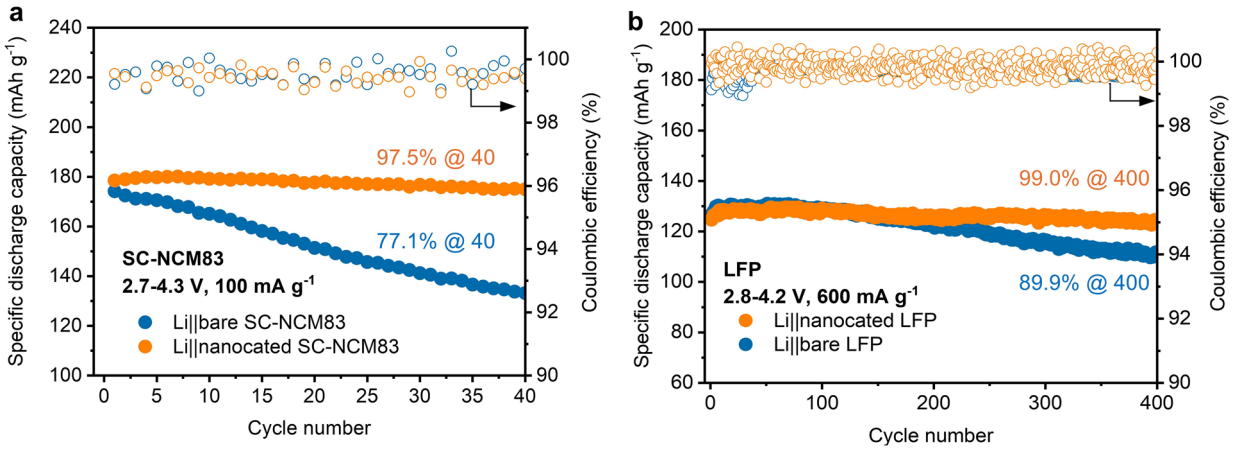
Extended Data Fig. 3 | Bulk Ni K-edge XAS and EXAFS analyses of bare and nanocoated Ni90-based positive electrodes before and after galvanostatic cycling in lithium metal coin cells at 200 mA g^{-1} in the 2.7 – 4.4 V cell potential range at 25 ± 2 °C. a. Normalized Ni K-edge XANES spectra of four representative samples: bare fresh, bare cycled, nanocoated fresh, and nanocoated cycled, compared with NiO and $LiNiO_2$ references. Successful normalization is confirmed by the consistent pre-edge baselines approaching 0 and post-edge plateaus approaching 1 across all spectra, ensuring reliable comparison of edge and white-line (WL) positions. **b.** Enlarged XANES results of bare fresh, bare cycled, coated fresh, and coated cycled samples, highlighting the edge position shift upon cycling. The enlarged edge region (inset) shows that the edge energy values (E_0) shift from 8341.8 eV (bare and nanocoated fresh) to 8342.0 eV (coated cycled) and 8342.9 eV (bare cycled), indicating increased Ni valence after cycling. **c.** Enlarged pre-edge region (~8330–8336 eV) attributed to 1 s → 3 d transitions and **d.** Fourier-transformed k^3-weighted EXAFS spectra of the four samples. The Ni–O and Ni–TM peaks remain well-defined for nanocoated samples, while bare cycled samples show dampened amplitudes, indicating more pronounced structural disorder. The 'fresh' state means the particle samples prior to cell assembly. Meanwhile, the 'cycled' state means the active material particles collected from positive electrodes that have been cycled in Li metal coin cells for 200 cycles at 200 mA g^{-1} and 25 ± 2 °C in the cell potential range of 2.7 - 4.4 V, followed by a final discharge at 20 mA g^{-1} to 2.7 V.

https://doi.org/10.1038/s41565-026-02224-y



Extended Data Fig. 4 | Ex situ post-mortem surface analyses of the cycled Ni90-based positive electrodes. The 'cycled' state means the electrode/active material particles collected from positive electrodes that have been cycled in Li metal coin cells for 200 cycles at 200 mA g^{-1} and 25 ± 2 °C in the cell potential range of 2.7 - 4.4 V, followed by a final discharge at 20 mA g^{-1} to 2.7 V. **a, b**, TEM images with corresponding Fluorine (F) EDS elemental mappings for the bare cycled (**a**) and the nanocoated cycled sample (**b**). **c, d**, High resolution TEM images of the surface regions and local inverse Fast Fourier Transformation (iFFT) images of the marked areas for the bare cycled (**c**) and nanocoated cycled (**d**) Ni90-based active material particle samples. **e-f**, TOF-SIMS 3D images of the PO^- (products from electrolyte decomposition) and NiO_2^-/PO^- overlay 3D images of bare cycled (**e**) and nanocoated cycled (**f**) Ni90-based positive electrodes. Note that the NiO_2^- signals are from the bulk Ni90 material and therefore represent the bulk component. **g**, TOF-SIMS depth profile of NiO_2^- (bulk), PO^- and LiF_2^- (electrolyte decomposition products) acquired from the bare cycled and nanocoated cycled positive electrodes. The results reveal decreased surface degradation in nanocoated samples. **h**, A schematic illustration of the suppressed crosstalk mechanism enabled by the polymer nanocoating.

https://doi.org/10.1038/s41565-026-02224-y



Extended Data Fig. 5 | Application of shape-memory polymer nanocoating for cyclability enhancement of single-crystal NCM83 (SC-NCM83) and $LiFePO_4$ (LFP) in Li metal coin cell configuration. a, capacity retention rate of Li | |nanocoated SC-NCM83 and Li | |bare SC-NCM83 over 40 cycles between 2.7 to 4.3 V at 100 mA g^{-1} and 25 ± 2 °C. The retention rate values are calculated based on the first specific discharge capacity at 100 mA g^{-1}, by taking the ratio of capacity at the final cycle to that at the first cycle (excluding the initial three formation cycles at 20 mA g^{-1}). **b**, Capacity retention rate of Li | |nanocoated LFP and Li | |bare LFP coin cells over 400 cycles between 2.7 to 4.2 V at 600 mA g^{-1} and 25 ± 2 °C. The retention rate values are calculated using the first specific discharge capacity at 600 mA g^{-1}, by taking the ratio of capacity at the final cycle to that at the first cycle (excluding the initial three formation cycles at 20 mA g^{-1}).